High-amplitude water-level fluctuations at the end of the Mediterranean Messinian Salinity Crisis: Implications for gypsum formation, connectivity and global climate

F. Andreetto, R. Flecker, G. Aloisi, A. M. Mancini, L. Guibourdenche, S. de Villiers, W. Krijgsman

HAL Id: insu-03776401

https://insu.hal.science/insu-03776401

Submitted on 13 Sep 2022

High-amplitude water-level fluctuations at the end of the Mediterranean Messinian Salinity Crisis: Implications for gypsum formation, connectivity and global climate

F. Andreetto [a],*, R. Flecker [b], G. Aloisi [c], A.M. Mancini [d], L. Guibourdenche [c], S. de Villiers [e], W. Krijgsman [a]

[a] Department of Earth Sciences, Utrecht University, Budapestlaan 17, Utrecht 3584 CD, the Netherlands
[b] BRIDGE, School of Geographical Sciences and Cabot Institute, University of Bristol, University Road, Bristol BS8 1SS, UK
[c] Université de Paris, Institut de physique du globe de Paris, CNRS, F-75005 Paris, France
[d] Dipartimento di Scienze della Terra, Università di Torino, Via Valperga Caluso 35, 10125, Torino, Italy
[e] AEON-ESSRI (Africa Earth Observatory Network-Earth Stewardship Science Research Institute), Nelson Mandela University, Port Elizabeth, South Africa

ABSTRACT

The formation and dissolution of salt giants impacts ocean chemistry on thousand-million year timescales. Gypsum precipitation and weathering changes the oceanic calcium concentration with implications for the carbon cycle and global temperatures. However, the connectivity of salt giants with the global ocean is necessarily restricted, making the timing of Ca^{2+} extraction and return more uncertain. Here we reconstruct the final phase of gypsum precipitation of the Late Miocene Mediterranean Salt Giant using micropaleontology, sedimentology and $^{87}Sr/^{86}Sr$ analyses on the most complete record preserved at Eraclea Minoa on Sicily and explore its implications for global climate. Precessional gypsum-marl couplets (Upper Gypsum) characterize the last 200 kyrs (Stage 3) of the Messinian Salinity Crisis (MSC; 5.97–5.332 Ma) in both intermediate (500–1000 m) and deep (>1000 m) Mediterranean basins. The interbedded selenitic gypsum layers contain well-preserved calcareous nannofossil assemblages dominated by *Reticulofenestra minuta*, a marine species which tolerates stressful conditions. Marine water is also required to explain the gypsum $^{87}Sr/^{86}Sr$ data, which describe a small range of ratios (0.708704–0.708813) lower than coeval ocean water. Mass-balance calculations indicate that during gypsum precipitation, the Atlantic made up ≤20% of a Mediterranean ("Lago-Mare") water mass dominated by low salinity discharge from large river systems and Eastern Paratethys. This suggests episodic extraction of calcium and sulfate ions from the ocean throughout MSC Stage 3. The marls commonly contain shallow (30–100 m) brackish-water ostracods of Parathethyan (Black Sea) origin. Marls with Parathethyan ostracods are also found in both marginal (<500 m) and deep Mediterranean settings. This indicates that marl-deposition was not synchronous across the basin, but that it occurred in intermediate and deep basins during base-level lowstands at insolation minima and on the shallow Mediterranean margins during insolation maxima-driven highstands. These high-amplitude base-level fluctuations exposed the evaporites to weathering, but ponded the products in the Mediterranean basin until reconnection occurred at the beginning of the Pliocene.

1. Introduction

Recent modeling of evaporite weathering and deposition suggests that, alongside the well-established silicate weathering and carbonate sedimentation feedback mechanisms, the formation and dissolution of giant calcium sulfate deposits may be an episodic driver of thousand-million year timescale changes in the carbon cycle (Shields and Mills, 2020). Salt giants have formed only episodically in Earth history, typically as a consequence of the tectonic restriction (opening or closing) of the connection between the global ocean and a mid-latitude marginal marine basin (Warren, 2016). Model experiments simulate the atmospheric CO_2 and temperature consequences of evaporite deposition and weathering events assuming a constant oceanic supply of Ca^{2+} and SO_4^{2-} ions

* Corresponding author.
  E-mail address: f.andreetto@outlook.it (F. Andreetto).

to the marginal basins, or a constant riverine Ca^{2+} and SO_4^{2-} flux from continental weathering, both lasting an estimated 1 million years (Shields and Mills, 2020). The heterogenous geological record of these salt giants, however, suggests that the ocean-marginal basin connectivity must have varied considerably (Warren, 2016), impacting the duration and intensity of ion fluxes in relation to evaporite precipitation and weathering during the formation of a salt giant. Reconstructing, the nature and timing of that variable connectivity, its relationship with gypsum precipitation and base-level changes is a critical step in quantifying the importance of this mechanism in driving carbon cycle change.

The most recent of the Earth's salt giants accumulated in the Mediterranean during the Messinian Salinity Crisis (MSC; 5.97–5.332 Ma). This formed as a consequence of Late Miocene tectonic uplift of the Gibraltar region which restricted marine exchange between the Mediterranean Basin and the Atlantic Ocean (e.g. Krijgsman et al., 2018). The Mediterranean's environmental response was dramatic, resulting in the precipitation of >1 million km^3 of evaporites (e.g. Roveri et al., 2014a). Three evaporitic episodes with different connectivity configurations have been distinguished (Roveri et al., 2014a): Stage 1, dominated by gypsum-marl couplets which are thought to have been deposited during restricted two-way Atlantic-Mediterranean exchange (e.g. Reghizzi et al., 2018); Stage 2 comprises an up to 2 km thick halite layer resulting from Atlantic inflow but no Mediterranean outflow (e.g. Krijgsman et al., 2018); and Stage 3 in which gypsum alternates with brackish-water, ostracod-bearing marls where the connectivity scenario is controversial (Andreetto et al., 2021a). It has proved difficult to explain both the outcrop data, which mostly suggest a relatively full Mediterranean, and evidence from deep-sea cores and seismics, which suggest low water conditions (see Andreetto et al., 2021a for summary). These different base level reconstructions have implications for Atlantic-Mediterranean connectivity at the end of the MSC and its impact on ocean chemistry.

Previous attempts to reconstruct Mediterranean hydrology, paleoenvironments and connectivity during Stage 3 have involved $^{87}Sr/^{86}Sr$ (Müller et al., 1990; Roveri et al., 2014b; García-Veigas et al., 2018) because water sources of different origin (i.e. ocean, lakes, rivers, groundwater) have distinct $^{87}Sr/^{86}Sr$ ratios (e.g. Reghizzi et al., 2018; Andreetto et al., 2021b, 2022; Bista et al., 2021). A solely geochemical approach to Stage 3 has proved inconclusive however, because more than one combination of potential source waters can result in the same geochemical signal. In this multi-proxy study, we combine new and existing sedimentological and paleontological observations with $^{87}Sr/^{86}Sr$ analyses on selenite gypsum crystals and ostracod valves from the Eraclea Minoa section (Caltanissetta Basin, Sicily; Fig. 1).

Eraclea Minoa is the most complete sedimentary record of Stage 3 exposed on land and previous works have described evidence of both Atlantic and Eastern Paratethys influence (Grossi et al., 2015; Vasiliev et al., 2017; García-Veigas et al., 2018). The succession shows strong precessional cyclicity from which an astronomical age model has been derived (van der Laan et al., 2006; Manzi et al., 2009). Unlike age-equivalent marginal exposures, which are dominated by continental clastics, the Caltanissetta Basin was, during Stage 3, at intermediate depths (500-1500 mbsl) and accumulated both gypsum and ostracod-bearing marls, allowing the Sr isotopic characterization of both lithological elements. This dataset allows us to reconstruct Stage 3 connectivity and consider its impact on Late Miocene ocean biogeochemistry and climate.

2. Materials and methods

The Eraclea Minoa section (37°23'36"N, 13°17'10.38"E) is ∼223 m-thick and comprises seven gypsum-marl alternations (Fig. 2). This Upper Gypsum succession is overlain sequentially by the Are-

nazzolo Fm., a ∼6-7 m-thick fine to medium-grained sandstone, and the Pliocene Trubi marls (Fig. 2). Field work to log and sample the Eraclea Minoa section was undertaken in Spring 2001 and September 2020 and 2021.

Selenitic gypsum can preserve biomineralized structures (Pellegrino et al., 2021), so twenty selenite crystals were selected from gypsums II to VII for micropaleontological screening. Crystals were cleaned of surface dirt using a brush and MilliQ purified water, sliced with a cleaned box cutter into 1-2 mm-thick splits and qualitatively analyzed, prior to carbon-coating the slices. Samples were then analyzed at the Electron Microscopy Centre at Utrecht University using a JEOL Neoscope II JCM-6000 table-top SEM equipped with an energy-dispersive X-ray spectroscopy (EDS) and Electron Probe Microanalyser JEOL JXA 8530F.

We expanded the available ostracod and gypsum $^{87}Sr/^{86}Sr$ dataset at Eraclea Minoa (Grossi et al., 2015; García-Veigas et al., 2018) with 43 additional isotopic ratios on gypsums (39) and *Cyprideis agrigentina* valves from cycle 3 (4). Sample preparation and data acquisition followed standard procedures for gypsum (Reghizzi et al., 2018) and ostracods (Bista et al., 2021; Andreetto et al., 2022). The more vitreous selenites and balatino gypsum chips were mechanically isolated, washed with MilliQ-water and micromilled with a hand drill avoiding impurities trapped within crystals. 10 mg of gypsum powder was digested in 1M ammonium acetate, centrifuged with MilliQ-water, dried overnight at 120 °C on a hot plate, redissolved in 3M HNO_3, centrifuged and refluxed on the hot plate. 6-7 adult valves of *C. agrigentina* were hand-picked under an optical microscope, repeatedly rinsed with MilliQ-water and methanol to remove potential contaminants (clay particles and organic material), dissolved in 300 μl of 0.1 M of HNO_3 and dried at 120 °C. Strontium of all samples was isolated using 100 μl of pre-cleaned Sr-Spec resin and loaded onto rhenium filaments with a $TaCl_5$ activator solution. $^{87}Sr/^{86}Sr$ ratios from gypsums V and VI were measured in SUERC (University of Glasgow) on a VG Sector 54-30 mass spectrometer in dynamic multi-collection mode. Instrumental mass fractionation was corrected using an exponential law and $^{86}Sr/^{88}Sr=0.1194$. NIST SRM987 values over the period the measurements were carried out were: $^{87}Sr/^{86}Sr$ =0.710251T20 (2cS.D.), n=95. $^{87}Sr/^{86}Sr$ ratios from the ostracods and gypsums I-IV and VII were measured at the Bristol Isotope Group Facilities (University of Bristol) on a Thermo-Finnigan Triton thermal ionization mass spectrometer using a multi-dynamic 'triple jump' method. The average $^{87}Sr/^{86}Sr$ is based on 200 ratios. The mean $^{87}Sr/^{86}Sr$ values of nine NIST SRM 987 analyzed during this session was 0.710245 ± 0.000006267 and that of four NIST SRM 987 which have undergone chemical purification (mean 0.710268 ± 0.0000236925) are in good agreement with the accepted values of SRM 987 of 0.710250.

3. Results

3.1. Sedimentological description of a typical UG cycle

Manzi et al. (2009) described three repeated facies associations of the Upper Gypsum at Eraclea Minoa: two distinct gypsum-dominated facies associations (B and C) and a single gypsum-free facies association (A). On the basis of more detailed lithological and faunal analysis, we divide their facies association A into two sub-units A and D.

Our sub-unit A, arbitrarily chosen as the base of the lithological cycle, comprises cm- to dm-thick beds of greenish, homogeneous marls interbedded with white laminated diatomites (Figs. 3c-d). This sub-unit, typically 1-2 meters thick, occurs immediately beneath the gypsum-bearing sequence (Figs. 2, 3b-c). Sub-unit D, at the top of the cycle, is found directly above the gypsum and consists of gray marls intercalated with cm- to dm-thick siltstones and
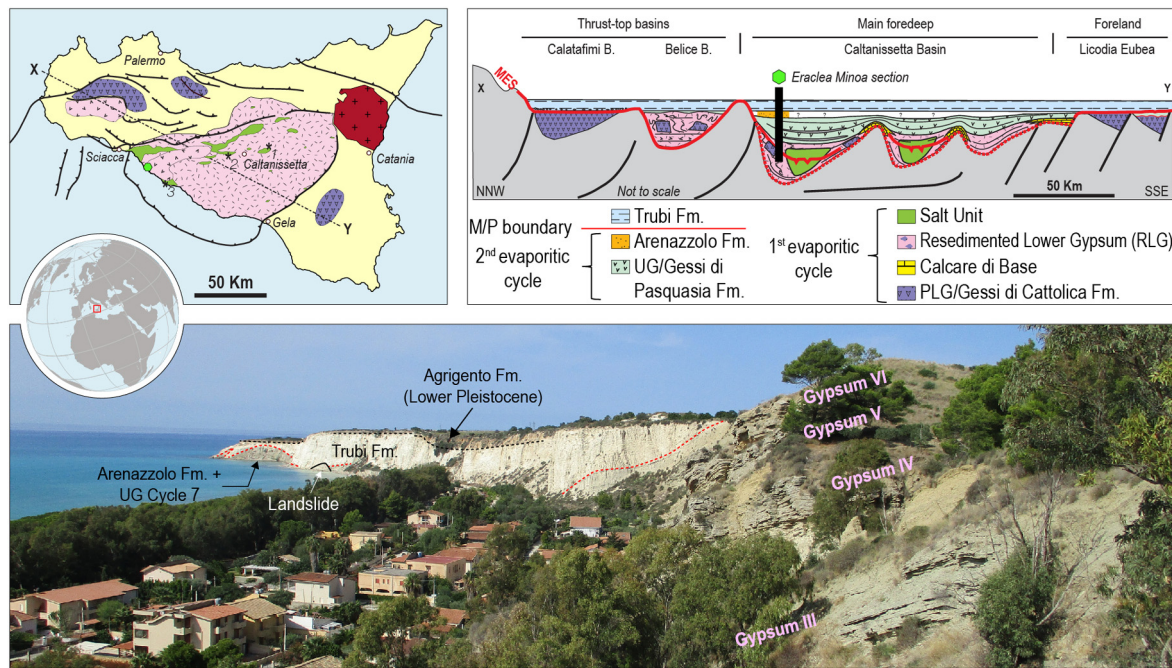
Fig. 1. Simplified geological map of Sicily (upper left figure; modified from Manzi et al., 2021) and NW-SE-oriented geological cross section (upper right figure; modified from Manzi et al., 2021) showing the geographical and stratigraphic position of the Eraclea Minoa section, respectively. Asterisks in the upper left figure indicate the position of other sections mentioned in the text (1: Balza Soletta, Maniscalco et al., 2019; 2: Montedoro, Rouchy and Caruso, 2006; 3: Siculiana Marina, Caruso and Rouchy, 2006). Below is a panoramic view of (part of) the Eraclea Minoa section. Four gypsum beds (III, IV, V and VI) overlooking the Eraclea Minoa village stand out in the foreground. The cliff of Cattolica Eraclea/Capo Bianco in the background is mainly composed of the white marly deposits of the Pliocene Trubi Fm. unconformably overlain by the Agrigento Fm. of Lower Pleistocene age. Locally, the topmost part of the UG and/or the Arenazzolo Fm. crop out at the cliff foot.

litharenites (Figs. 2, 3h). The gypsum layers at Eraclea Minoa typically start with cm- to dm-thick beds of laminar (or balatino) and clastic gypsum (gypsarenites) alternating with greenish homogeneous marls (sub-unit B; Figs. 3c, e) and show a sharp change to rhythmic alternations of dm-thick layers of massive selenite and mm- to cm-thick greenish marls (sub-unit C; Fig. 3f). The balatino gypsum comprises alternating mm-thick gypsum cumulate layers with clay-rich horizons only a few hundreds of microns thick (Fig. 3e). The gypsarenites are commonly massive (Fig. 3e) with occasional sedimentary structures such as normal grading and horizontal lamination (Manzi et al., 2009). The selenite beds comprise bottom-grown, swallow-tail gypsum crystals (or selenites) oriented with the re-entrant angle of the twins upward (Fig. 3f). Crystal size is relatively uniform in individual beds, but increases vertically through sub-unit C, from cm-scale crystals at the base to several dm in length at the top. The geometry of the gypsum beds also changes upwards, from tabular (Fig. 3f) to domal or cauliflower-shaped (Fig. 3b). The resulting irregular upper surface (Fig. 3b) led some authors to interpret an episode of subaerial erosion (e.g. Rouchy and Caruso, 2006; Raad et al., 2021). However, no karstic features are observed in the Eraclea Minoa gypsums (see also Manzi et al., 2009).

At Eraclea Minoa, cycles 5, 6 and 7 all show a consistent facies sequence from the diatomite-bearing sub-unit A, through the cumulate and clastic gypsum sub-unit B, selenite-dominated sub-unit C, to the ostracod-bearing marls of sub-unit D (Fig. 2). Cycles 3 and 4 comprise sub-units B-D without the diatomaceous sub-unit A. Cycles 1 and 2 are poorly exposed with only sub-unit B visible in cycle 1 and C and D in cycle 2 and 3 (Fig. 2).

3.2. Micropaleontology

3.2.1. Ostracods in sub-unit D marls

Sub-unit D marls contain 25 ostracod species (Grossi et al., 2015). One of these, *C. agrigentina*, is of Mediterranean origin

(Grossi et al., 2015). All the others are endemic to Paratethys (Fig. 2; Stoica et al., 2016). The absence of Paratethyan ostracods in Mediterranean sediments prior to MSC Stage 3 and the occurrence here of well-preserved valves of different moult stages indicate that these ostracods are *in situ* (Grossi et al., 2015). In cycles 3, 6 and 7 there is a clear increase in ostracod diversity through sub-unit D from almost (cycle 7) or completely (cycle 3 and 6) monospecific assemblages of *C. agrigentina* (Biofacies 1) at the base to diverse communities of Paratethyan taxa (Biofacies 2) at the top (Fig. 2; Grossi et al., 2015). Planktic and benthic foraminifera have also been reported from sub-unit D's marls (Caruso and Rouchy, 2006). However, only *Ammonia tepida*, which like *C. agrigentina* dwells in euryhaline and shallow-water, is considered to be *in-situ* (Grossi et al., 2015). One of the three samples from a marl layer interbedded with selenites (sub-unit C) also contained valves of *C. agrigentina* and *Loxoconcha muelleri* (Fig. 2; Grossi et al., 2015). Analysis of a small number of marl samples from sub-unit A suggests that these sediments contain no ostracods (Fig. 2).

3.2.2. Calcareous nannofossils in selenitic gypsum

The Eraclea Minoa selenites display alternating turbid/dark and transparent laminae (Fig. 4a). SEM inspection of samples from layers II-VII reveals that the dark color is associated with abundant, closely packed calcareous nannofossils associated with a small detrital component, mostly clay and rare silt- and clay-sized euhedral halite crystals (Fig. 4b), which might result from drying out of fluid inclusions. Since the analyzed samples are slices of selenite crystals, we can confirm that these are microfossils embedded within the gypsum (Figs. 4b-d). Well preserved calcareous nannofossils comprising pristine platelets and intact coccospheres (Fig. 4e) are observed both in cavities (Figs. 4b-c, e-f) and within the undamaged parts of the crystals (Fig. 4d). Poorly preserved specimens including fragments and intact platelets with the central area missing are preferentially found in the cavities (Figs. 4b-c, f). However, the preservation of fine details on the platelets allows species-level
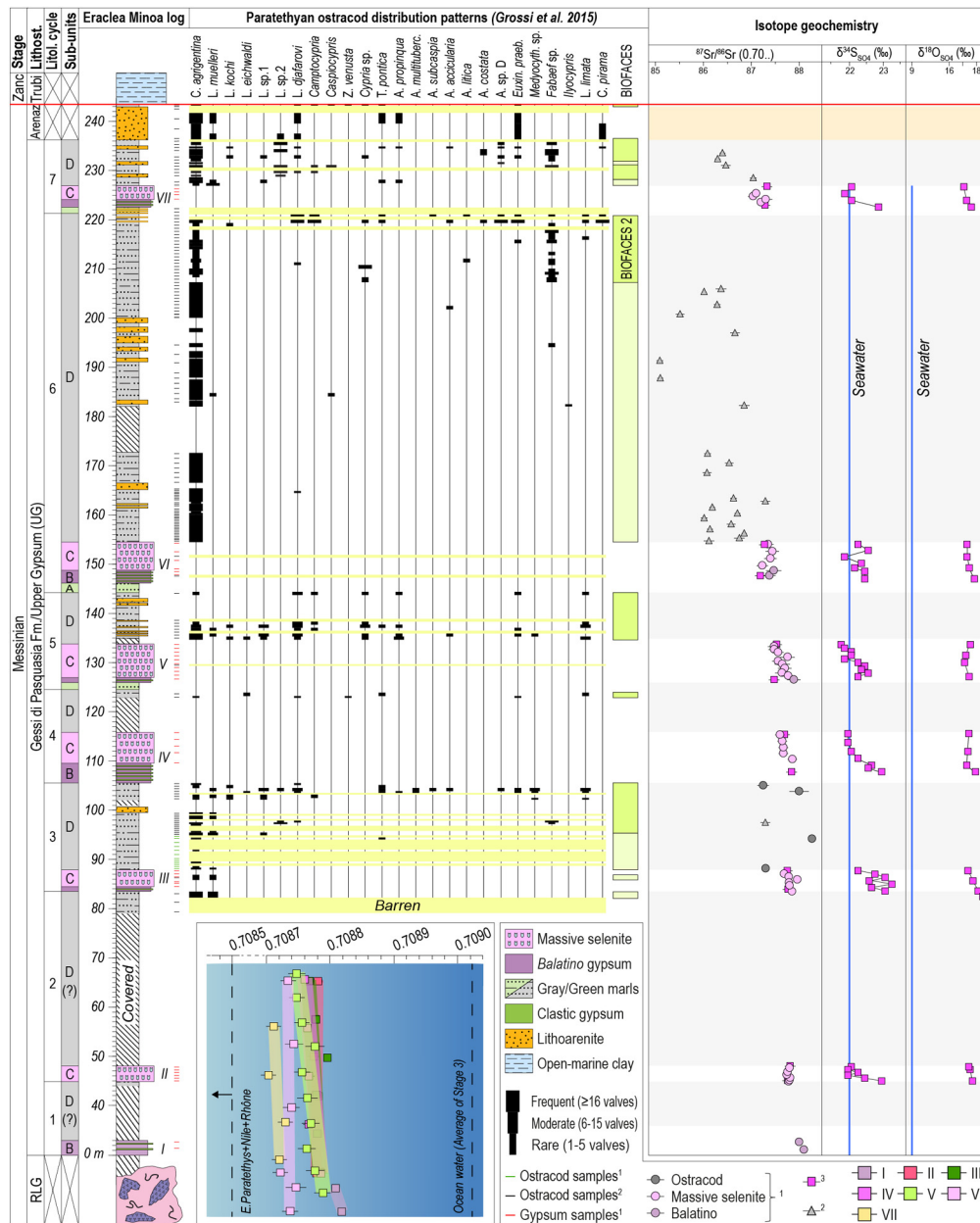
Fig. 2. Lithological log of the Eraclea Minoa section (modified from Manzi et al., 2009). An ostracod stratigraphic distribution chart (Fig. 2) was constructed integrating the results of Grossi et al. (2015) with seventeen marl samples from the base of cycle 3 provided by Elsa Gliozzi and Domenico Cosentino and prepared at the Earth Science Department of the Università degli Studi Roma Tre with standard micropaleontological methods of washing, sieving and drying. New and published (Grossi et al., 2015; García-Veigas et al., 2018) $^{87}Sr/^{86}Sr$ ratios measured on gypsum crystals and ostracod valves and sulfur and oxygen (in sulfate) isotope profiles from García-Veigas et al. (2018) are also plotted. The bottom diagram is a close view of the $^{87}Sr/^{86}Sr$ isotopic composition of the gypsum beds I-VII. Data are plotted against the coeval oceanic ratio (after McArthur et al., 2012) and the composition of a system mixing river water from Nile and Rhône (0.707427; Topper et al., 2011) and the Eastern Paratethys (0.7084-0.7085 during the latest Messinian; Grothe et al., 2020). The lack of overlap between gypsum and water data are evidence that the gypsum-precipitating water was a combination of all three sources mentioned above. (1): This study; (2): Grossi et al. (2015); (3): García-Veigas et al. (2018).

identification. *Reticulofenestra minuta* is by far the most abundant taxon forming dominant or monospecific assemblages (Figs. 4b-d). Rare specimens of *Reticulofenestra haqii*, *Reticulofenestra antarctica*, *Calcidiscus leptoporus*, *Coccolithus pelagicus*, *Helicosphaera carteri*, *Sphenolithus abies*, *Umbilicosphaera jafari* and *Chiasmolithus* sp. are also observed (Fig. 4f). All taxa with the exception of *Chiasmolithus* sp., which went extinct in the Chattian, have chronostratigraphic ranges that overlap with Stage 3.

3.3. Sr/⁸⁶Sr results

Gypsum samples are characterized by a narrow range of $^{87}Sr/^{86}Sr$ (0.708704-0.708813; Table 1, Fig. 2). These data are substan-

tially lower than $^{87}Sr/^{86}Sr$ ratios of coeval seawater (∼0.709022; McArthur et al., 2012) and consistent with published $^{87}Sr/^{86}Sr$ ratios from Eraclea Minoa (García-Veigas et al., 2018) and from selenites of the Siculiana Marina section (0.708700-0.708760; Keogh and Butler, 1999), ∼20 km to the SE (Fig. 1). Gypsum data from individual gypsum beds are either constant (II) or they show small-scale variability, commonly a decline from bottom to top (I, III–VII). There is also a small, but analytically resolvable decrease in $^{87}Sr/^{86}Sr$ ratios from the bottom of the section (Gypsum I) to the top (Gypsum VII).

The $^{87}Sr/^{86}Sr$ range of sub-unit D's ostracods is substantially larger than the gypsum (0.708510–0.708827; Fig. 2). Four of these samples (three in cycle 3 and one in cycle 7) have $^{87}Sr/^{86}Sr$ ratios
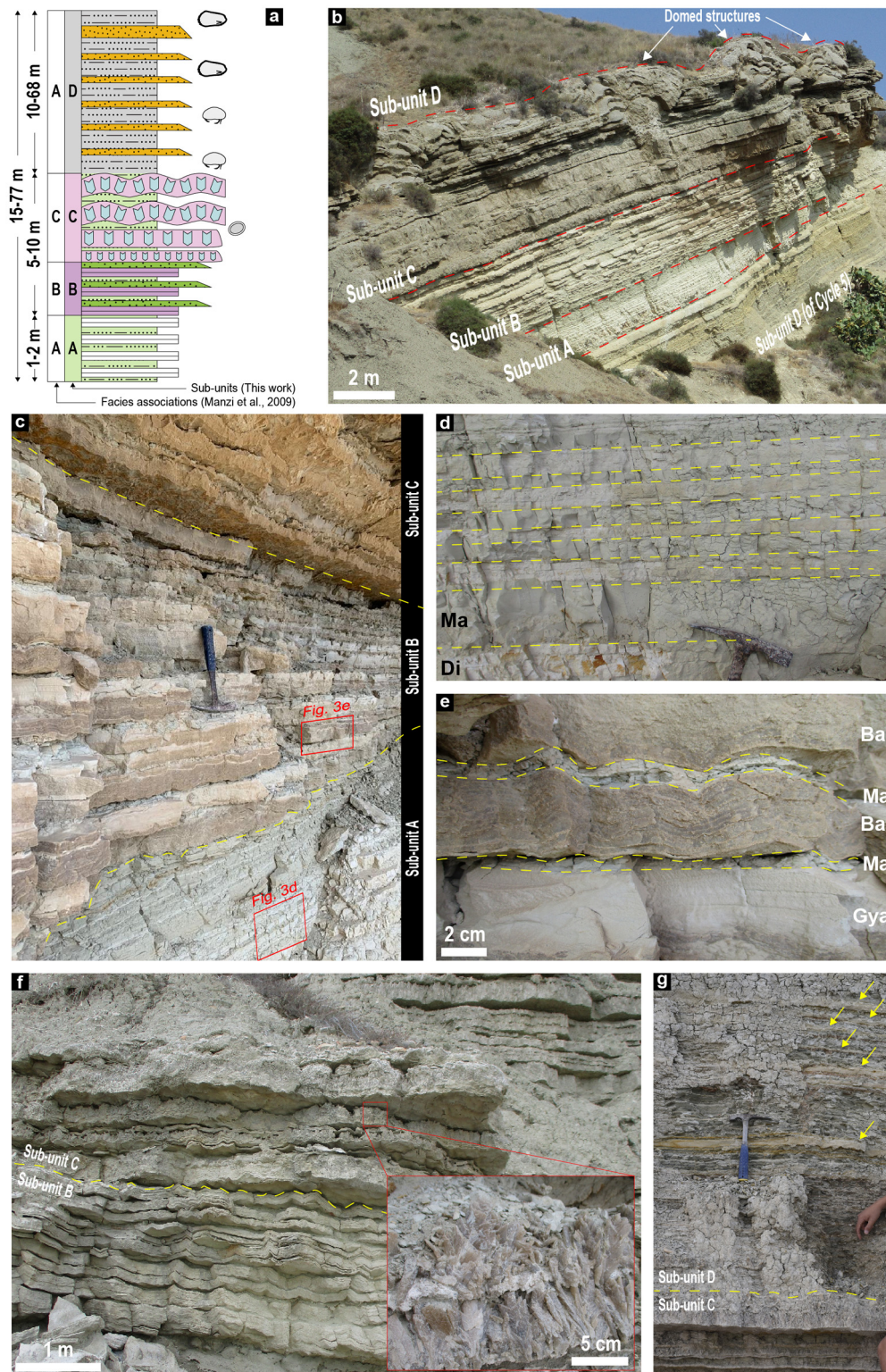
Fig. 3. a: Schematic representation of a complete UG depositional cycle. Four sub-units (A to D) are distinguished alongside the three facies associations of Manzi et al. (2009). See legend in Fig. 7a. **b:** Outcrop view of cycle 6 which contains all four sub-units. Note the sharp boundaries (red dashed lines) between the sub-units. **c:** Close up of sub-units A to C of cycle 5. Yellow dashed lines indicate the sub-unit boundaries. **d:** Alternations of white diatomites (Di) and greenish marls (Ma) in sub-unit A of cycle 5. **e:** Close-up of sub-unit B in cycle 5 showing planar-laminated gypsarenite (Gya), greenish marls (Ma) and balatino gypsum beds (Bal). The laminae of the balatino gypsum locally show small scale folding. **f-g:** Transition from sub-unit B to C (**f**) and sub-unit C to D (**g**) from cycle 7 as exposed along the beach at the foot of the cliff Cattolica Eraclea/Capo Bianco cliff. Yellow arrows in Fig. 3g point to brownish litharenites interbedded with gray marls of sub-unit D. (For interpretation of the colors in the figure(s), the reader is referred to the web version of this article.)
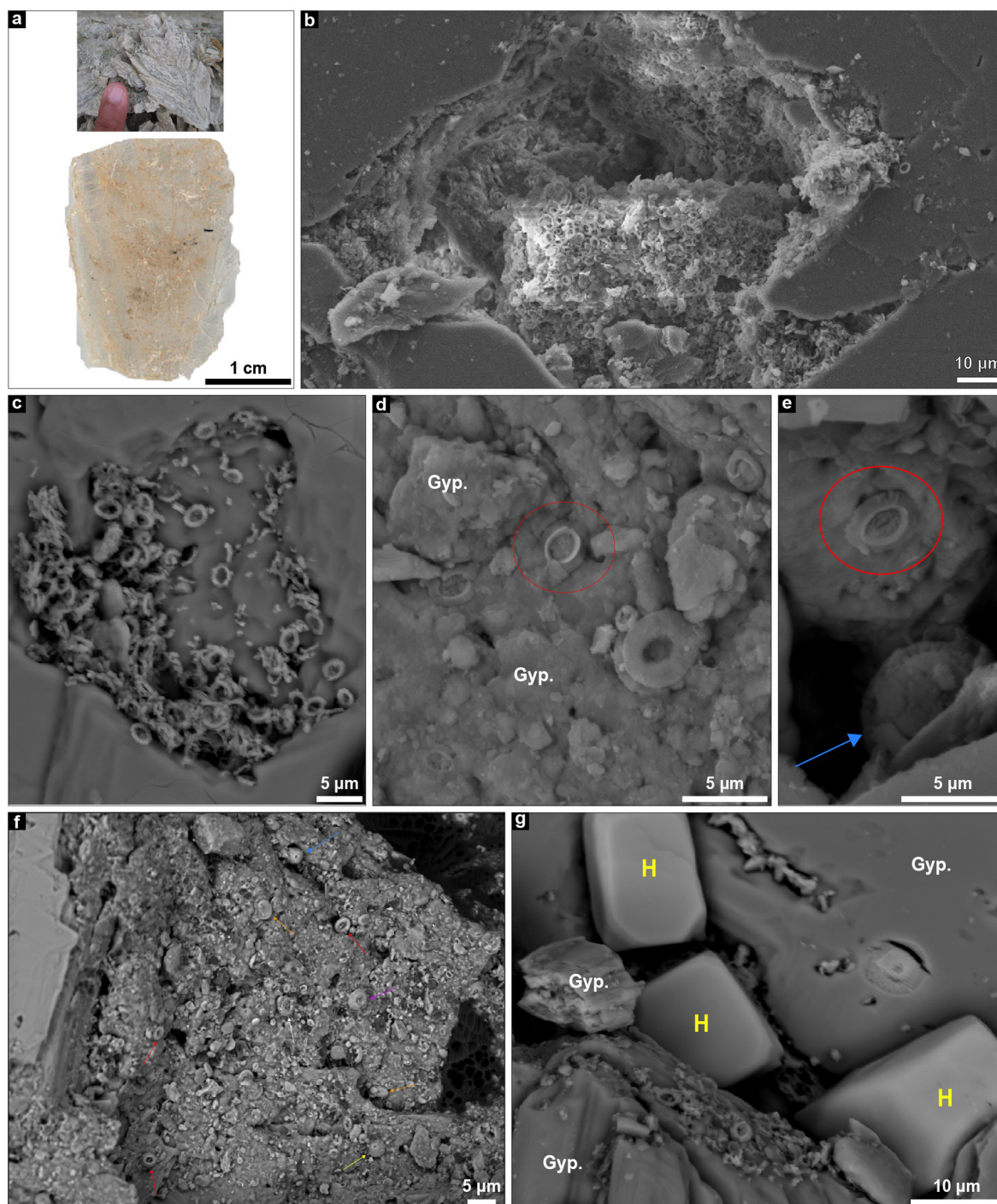
Fig. 4. SEM photomicrographs of calcareous nannofossils from Upper Gypsum selenitic crystals (**a**) of Eraclea Minoa. Platelets and coccospheres are better observable in cavities (**b-c**, **e-g**) and, to a lesser degree, where the crystal surface is pristine (**d**). The specimens can be regarded as embedded in the gypsum (gyp) since the analyzed surfaces are obtained after the removal of a portion of the crystal (see the materials and methods section for insights). **a:** Swallow-tail selenite crystal from the second Upper Gypsum bed (fingertip for scale) and an example of a sliced selenite crystal (from gypsum VII) prepared for SEM. This thin gypsum slice shows the alternation of clear and turbid (brownish) laminae which are rich in calcareous nannofossils. **b-c:** Monospecific accumulation of *Reticulofenestra minuta* with relatively well-preserved platelets. **d-e:** Oligospecific assemblages of *R. minuta* and *R. haqii* (red circle). The blue arrow in Fig. 4e points to an intact coccosphere of *R. minuta*. **f:** Oligospecific calcareous nannofossil assemblage including *R. haqii* (red arrows), *Calcidiscus leptoporus* (yellow arrow), *Helicosphaera carteri* (orange arrows), *Coccolithus pelagicus* (violet arrow) and *Chiasmolitus* sp. (white arrow). The remaining unmarked plates all belong to *R. minuta*. A coccosphere of *R. minuta* is also visible in the top of the picture (blue arrow). **g:** Euhedral crystals of halite (H) in a gypsum crack. The plates of calcareous nannofossils belong to the genus *R. minuta*.

higher or equivalent to the range of the gypsums; the remaining 25 have ratios lower than the gypsums. In the lowermost 52 m of sub-unit D of Cycle 6, which has the highest sampling resolution, fluctuations in ^{87}Sr/^{86}Sr are both high frequency and high-amplitude.

4. Discussion

4.1. Coccoliths in gypsums

The presence of marine calcareous nannofossils within the Era-clea Minoa UG selenites indicates that they were settling out from

suspension while gypsum was growing on the basin floor. Fragmented, poorly preserved platelets with an empty central area are present, indicating that some degree of physical reworking took place. The single occurrence of *Chiasmolithus* sp. corroborates this. However, fragmented platelets are preferentially found in large, irregularly-shaped cavities (Figs. 4b-c). When pristine areas of the gypsum slices (Fig. 4d) or small cracks (Fig. 4e) are inspected, preservation is better and complete coccospheres are observed. These delicate structures do not typically withstand erosion and transport intact. Other observations that are difficult to reconcile with an entirely reworked origin include the scarcity of terrigenous particles, the absence of bioclasts other than coccoliths and the limited diversity of these assemblages, which are solely or largely dominated by *R. minuta* (Figs. 4b, c-d). The absence of other marine organisms is indicative of a stressed environment in which only a few species could thrive. Interestingly, the dominant species, *R. minuta*, is regarded as an opportunistic taxon capable of inhabiting a wide range of salinity conditions, from brackish to hypersaline (Auer et al., 2014). Taken together, these data suggest that while minor reworking occurred, at least *R. minuta*, which is abundant, thrived in the Caltanissetta Basin during selenite precipitation. Being that *R. minuta* is of a marine origin, its finding in the Stage 3 selenites of Eraclea Minoa indicates that the Caltanissetta Basin was, at least during the evaporitic phases, supplied with Atlantic seawater. The seawater-like $\delta^{34}S_{SO4}$ signature of the gypsums is consistent with the nannofossil-based conclusion (Fig. 2; Manzi et al., 2009; García-Veigas et al., 2018).

Monospecific assemblages of dwarfed nannofossils, identified as likely belonging to the genus *Reticulofenestra*, have also been described from the thin calcareous laminae of the balatino lithofacies in ODP Site 653B (Tyrrhenian Basin; Pierre and Rouchy, 1990) and in the Montedoro section (Rouchy and Caruso, 2006), located some 50 km to the NE of Eraclea Minoa, and from the balatino lithofacies in ODP Site 968A (Eratosthenes Seamount; Blanc-Valleron et al., 1998), where again they are embedded within the gypsum crystals themselves. These findings in gypsums from intermediate-deep settings to the east and west of the Caltanissetta Basin suggest that the Stage 3 gypsum subbasins of the Mediterranean may have been, at least during the evaporitic phases, part of a single, Atlantic-fed water body (which we refer to as "Lago-Mare"; see next section) typified by stressful environmental conditions (Fig. 6). The Western Alborán, Adriatic and North Aegean basins, which are Stage 3 gypsum-free, are likely to have been sealed off from the gypsum-forming Lago-Mare water mass due to the presence of dividing sills and to have maintained, for at least part of Stage 3, different water masses subject to independent base-level and hydrologic evolution (Fig. 6). Studies of the sedimentary and paleontological records of these basins support this conclusion (Pellen et al., 2017; Booth-Rea et al., 2018; Krijgsman et al., 2020).

4.2. $^{87}Sr/^{86}Sr$ characterization of the "Lago-Mare" water mass

The gypsum $^{87}Sr/^{86}Sr$ data at Eraclea Minoa (0.708704-0.708813; Fig. 2), like the Stage 3 gypsums elsewhere in the Mediterranean (<0.708850; Roveri et al., 2014b), have substantially lower ratios than coeval ocean water (~0.709022; McArthur et al., 2012). Modeled $^{87}Sr/^{86}Sr$ of mixtures of Atlantic seawater and circum-Mediterranean freshwater show that measurable deviations from the oceanic $^{87}Sr/^{86}Sr$ signature are achieved when river discharge constitutes at least 25% of the total water fluxes (Topper et al., 2014). The Upper Gypsum $^{87}Sr/^{86}Sr$ data therefore indicate that the Lago-Mare water mass was a marine water body strongly influenced by continental-derived sources with lower than marine $^{87}Sr/^{86}Sr$.

If Mediterranean base-level at times of gypsum precipitation was low enough to expose basin margin sediments, rivers drain-

ing these sediments may have influenced the water composition in Caltanissetta. Primary Lower Gypsum, both in situ (Stage 1) and reworked (Stage 2; Manzi et al., 2021), is abundant in the Caltanissetta Basin. Local rivers draining the margins may therefore have provided additional Ca^{2+} and SO_4^{2-}, but would have had relatively high $^{87}Sr/^{86}Sr$ (~0.7090; Lugli et al., 2010). However, the catchments of these rivers today are dominated by Meso-Cenozoic limestones, which would have produced lower $^{87}Sr/^{86}Sr$ (<0.7080).

On a more regional scale, the presence of ostracods derived from Eastern Paratethys suggests that this water body was a contributor of low $^{87}Sr/^{86}Sr$ non-marine water (0.7084-0.7085; Grothe et al., 2020) to the Mediterranean during Stage 3 (e.g. Andreetto et al., 2021a). Climate model simulations for the late Miocene show that the hydrological budget of the Eastern Paratethys was positive during the MSC (Marzocchi et al., 2016). This means that this low-salinity water flow to the Mediterranean was not restricted only to times of marl deposition, where the Paratethyan fauna is found, but was present also during the evaporitic phases. The Mediterranean's major rivers, including the Nile and Rhône (0.7060 and 0.7087 respectively; e.g. Topper et al., 2011), which today make up >80% of the total Mediterranean river discharge, are also likely to have contributed low $^{87}Sr/^{86}Sr$ water, along with North African fluvial systems that are currently dry (e.g. the Eosahabi River that flowed from Messinian Lake Chad), but for which there is evidence of late Miocene flow (Griffin, 2006).

Mass-balance calculations were used to explore the relative proportions of Sr^{2+} derived from the possible sources that explain the $^{87}Sr/^{86}Sr$ data at Eraclea Minoa (Fig. 5a). If we assume that water from Eastern Paratethys was characterized by river-like Sr concentrations (Figs. 5b-c), our model suggests that a maximum of ~20% Atlantic seawater is required to reproduce the gypsum $^{87}Sr/^{86}Sr$ data (Fig. 5b). This result is in agreement with the box model calculations of Topper et al. (2014) and points to the presence of a strongly diluted marine water mass with a restricted Atlantic-Mediterranean connection during Stage 3 gypsum formation.

Restricted ocean inflow can be provided by an Atlantic-Mediterranean gateway either as a one-way flow or with a parallel outflow. The two-way flow configuration facilitates the formation of gypsum because it entails a larger inflow of water (and ions) and keeps the salinity below halite saturation (Krijgsman and Meijer, 2008). The presence of gypsum and absence of large volumes of demonstrably in-situ halite in Stage 1 and 3 units (Roveri et al., 2014a; Andreetto et al., 2021a) is consistent with this scenario. However, two-way exchange requires Mediterranean base-level to be equal with the Atlantic sea-level (Krijgsman and Meijer, 2008), which means the marginal Mediterranean subbasins remain permanently submerged. This is the case in Stage 1. However, the evidence of substantial base-level change (section 4.5) and the frequent switching from subaqueous to continental sedimentation on the margins (Andreetto et al., 2021a, 2022) make persistent two-way exchange during the UG highly unlikely and support a small, unidirectional Atlantic input to the Mediterranean (Fig. 6). Existing box models simulations of the blocked outflow scenario result in rapid and voluminous halite precipitation (Krijgsman and Meijer, 2008). However, these simulations do not include the inflow of low-salinity water from Eastern Paratethys. One possibility is that inflow from Paratethys, with a small Atlantic contribution may have kept the Lago-Mare water mass below halite saturation, but allowed it, episodically, to achieve gypsum saturation.

4.3. Implications of UG cycles for base-level and insolation

Evaporite-marl alternations denote cycles of concentration and dilution of the water mass with respect to evaporitic ions and are commonly associated with water level changes (Lowenstein,

Table 1

Compilation of the ^{87}Sr/^{86}Sr ratios from the Eraclea Minoa section plotted in Fig. 2. Asterisks indicate that the analyzed samples are not assigned by the original authors to one of the sub-units distinguished in this work.

Cycle	Sample	Sample type	Sub-unit	Stratigraphic height (m)	^{87}Sr/^{86}Sr	Error	Reference
7	EM 8-11	Calcite (*C. Agrigentina*)	D	233,5	0.70864	6E-06	Grossi et al. (2015)
7	EM 8-9	Calcite (*C. Agrigentina*)	D	232	0.70863	8E-06	Grossi et al. (2015)
7	EM 8-7	Calcite (*C. Agrigentina*)	D	231	0.708647	1E-05	Grossi et al. (2015)
7	EM 8-3	Calcite (*C. Agrigentina*)	D	228,5	0.708704	7E-06	Grossi et al. (2015)
7	EM-44	Gypsum (Selenite)	B*	227*	0.708732	1E-05	García-Veigas et al. (2018)
7	G7-8	Gypsum (Selenite)	C	226.2	0.708710	8.40E-06	This work (Bristol)
7	G7-6	Gypsum (Selenite)	C	225.7	0.708704	1.08E-05	This work (Bristol)
7	G7-4	Gypsum (Selenite)	C	225	0.708730	1.40E-05	This work (Bristol)
7	G7-1	Gypsum (Selenite)	C	224.2	0.708720	6.50E-06	This work (Bristol)
7	EM-41	Gypsum (Balatino)	B*	223*	0.708729	1E-05	García-Veigas et al. (2018)
6	EM 7-10	Calcite (*C. Agrigentina*)	D	206	0.708637	1.1E-05	Grossi et al. (2015)
6	EM 7-9	Calcite (*C. Agrigentina*)	D	205	0.708602	2E-06	Grossi et al. (2015)
6	EM 7-5	Calcite (*C. Agrigentina*)	D	202.8	0.708629	7E-06	Grossi et al. (2015)
6	EM 7-2	Calcite (*C. Agrigentina*)	D	201	0.708552	9E-06	Grossi et al. (2015)
6	EM 6"-20	Calcite (*C. Agrigentina*)	D	197	0.708666	1E-05	Grossi et al. (2015)
6	EM 6"-17	Calcite (*C. Agrigentina*)	D	191	0.708510	7E-06	Grossi et al. (2015)
6	EM 6"-14a	Calcite (*C. Agrigentina*)	D	188	0.708511	5E-06	Grossi et al. (2015)
6	EM 6"-8	Calcite (*C. Agrigentina*)	D	182.3	0.708685	1.1E-05	Grossi et al. (2015)
6	EM 6"-7	Calcite (*C. Agrigentina*)	D	172.3	0.708609	7E-06	Grossi et al. (2015)
6	EM 6"-5	Calcite (*C. Agrigentina*)	D	170.3	0.708654	9E-06	Grossi et al. (2015)
6	EM 6"-3	Calcite (*C. Agrigentina*)	D	168.3	0.708608	9E-06	Grossi et al. (2015)
6	EM 6'-27	Calcite (*C. Agrigentina*)	D	163.3	0.708663	7E-06	Grossi et al. (2015)
6	EM 6'-25	Calcite (*C. Agrigentina*)	D	162.8	0.708729	1E-05	Grossi et al. (2015)
6	EM 6'-22b	Calcite (*C. Agrigentina*)	D	161.3	0.708619	5E-06	Grossi et al. (2015)
6	EM 6'-19	Calcite (*C. Agrigentina*)	D	160.3	0.708671	5E-06	Grossi et al. (2015)
6	EM 6'-16	Calcite (*C. Agrigentina*)	D	159.3	0.708602	7E-06	Grossi et al. (2015)
6	EM 6'-12	Calcite (*C. Agrigentina*)	D	158.3	0.708658	9E-06	Grossi et al. (2015)
6	EM 6'-9	Calcite (*C. Agrigentina*)	D	157.3	0.708614	5E-06	Grossi et al. (2015)
6	EM 6'-6	Calcite (*C. Agrigentina*)	D	156.3	0.708685	5E-06	Grossi et al. (2015)
6	EM 6'-3	Calcite (*C. Agrigentina*)	D	155.3	0.708675	1E-05	Grossi et al. (2015)
6	EM 6'-1	Calcite (*C. Agrigentina*)	D	154.8	0.708612	1.1E-05	Grossi et al. (2015)
6	EM-39	Gypsum (Balatino)	C*	154.2*	0.708724	1E-05	García-Veigas et al. (2018)
6	EM-84	Gypsum (Selenite)	C	154.2	0.708735	1.2E-05	This work (Glasgow)
6	EM-78	Gypsum (Selenite)	C	152.5	0.708744	1.4E-05	This work (Glasgow)
6	EM-76	Gypsum (Selenite)	C	151	0.708740	1.3E-05	This work (Glasgow)
6	EM-69	Gypsum (Selenite)	C	149	0.708723	1.2E-05	This work (Glasgow)
6	EM-64	Gypsum (Balatino)	B	148.5	0.708747	1.3E-05	This work (Glasgow)
6	EM-63	Gypsum (Balatino)	B	148	0.708738	1.3E-05	This work (Glasgow)
6	EM-33	Gypsum (Balatino)	B*	148*	0.708719	1E-05	García-Veigas et al. (2018)
5	EM-31	Gypsum (Selenite)	C*	133.8*	0.708751	1E-05	García-Veigas et al. (2018)
5	EM-58	Gypsum (Selenite)	C	133.8	0.708748	1.3E-05	This work (Glasgow)
5	EM-56	Gypsum (Selenite)	C	132.8	0.708748	1.2E-05	This work (Glasgow)
5	EM-54	Gypsum (Selenite)	C	132.2	0.708756	1.2E-05	This work (Glasgow)
5	EM-52	Gypsum (Selenite)	C	131.3	0.708776	1.4E-05	This work (Glasgow)
5	EM-38	Gypsum (Selenite)	C	130.6	0.708756	1.3E-05	This work (Glasgow)
5	EM-36	Gypsum (Selenite)	C	129.8	0.708765	1.6E-05	This work (Glasgow)
5	EM-34	Gypsum (Selenite)	C	129	0.708770	1.4E-05	This work (Glasgow)
5	EM-33	Gypsum (Selenite)	C	128.2	0.708764	1.4E-05	This work (Glasgow)
5	EM-31	Gypsum (Selenite)	C	127.5	0.708777	1.4E-05	This work (Glasgow)
5	EM-25	Gypsum (Balatino)	B	126.6	0.708789	1.4E-05	This work (Glasgow)
5	EM-22	Gypsum (Balatino)	B*	126.6*	0.708747	1E-05	García-Veigas et al. (2018)
4	EM-20	Gypsum (Selenite)	C*	115.8*	0.708769	1E-05	García-Veigas et al. (2018)
4	G4-10	Gypsum (Selenite)	C	115.8	0.70876	6.21E-06	This work (Bristol)
4	G4-8	Gypsum (Selenite)	C	114.5	0.708765	5.23E-06	This work (Bristol)
4	G4-6	Gypsum (Selenite)	C	113	0.708767	9.79E-06	This work (Bristol)
4	G4-4	Gypsum (Selenite)	C	111.5	0.708767	8.32E-06	This work (Bristol)
4	G4-1	Gypsum (Selenite)	C	109.5	0.708786	3.89E-06	This work (Bristol)
4	EM-13	Gypsum (Balatino)	B*	108*	0.708783	1E-05	García-Veigas et al. (2018)
3	EM4-19	Calcite (*C. Agrigentina*)	D	105	0.708725	1.2E-05	This work (Bristol)
3	EM4-17	Calcite (*C. Agrigentina*)	D	104	0.7088	3E-05	This work (Bristol)
3	EM4-7	Calcite (*C. Agrigentina*)	D	97	0.708729	1E-05	Grossi et al. (2015)
3	EM4-0K	Calcite (*C. Agrigentina*)	D	94	0.708827	6.30E-06	This work (Bristol)
3	EM4-00a	Calcite (*C. Agrigentina*)	D	88	0.70873	1.2E-05	This work (Bristol)
3	EM-12	Gypsum (Selenite)	C*	88*	0.708773	1E-05	García-Veigas et al. (2018)
3	G3-11	Gypsum (Selenite)	C	87.70	0.708769	6.069E-06	This work (Bristol)
3	G3-9	Gypsum (Selenite)	C	87.05	0.708778	6.364E-06	This work (Bristol)
3	G3-7	Gypsum (Selenite)	C	86.4	0.708796	7.27E-06	This work (Bristol)
3	G3-4	Gypsum (Selenite)	C	85.5	0.708779	5.60E-06	This work (Bristol)
3	G3-3	Gypsum (Selenite)	C	85.15	0.708780	6.18E-06	This work (Bristol)
3	G3-1	Gypsum (Selenite)	C	84.5	0.708785	6.12E-06	This work (Bristol)
3	EM-7	Gypsum (Balatino)	B*	84*	0.708777	1E-05	García-Veigas et al. (2018)
2	EM-6	Gypsum (Selenite)	C*	48*	0.708780	1E-05	García-Veigas et al. (2018)
2	G2-11	Gypsum (Selenite)	C	47.75	0.708780	5.83E-06	This work (Bristol)
2	G2-9	Gypsum (Selenite)	C	47.2	0.708776	7.05E-06	This work (Bristol)
2	G2-7	Gypsum (Selenite)	C	46.65	0.708774	8.25E-06	This work (Bristol)
2	G2-5	Gypsum (Selenite)	C	46.1	0.708781	4.77E-06	This work (Bristol)
2	G2-3	Gypsum (Selenite)	C	45.55	0.708780	7.67E-06	This work (Bristol)
2	G2-1	Gypsum (Selenite)	C	45	0.708778	6.47E-06	This work (Bristol)
2	EM-2(a)	Gypsum (Balatino)	C*	45*	0.708775	1E-05	García-Veigas et al. (2018)
1	Cum-5	Gypsum (Balatino)	B	2.7	0.708800	5.5E-06	This work (Bristol)
1	Cum-3	Gypsum (Balatino)	B	1.5	0.708810	5.6E-06	This work (Bristol)

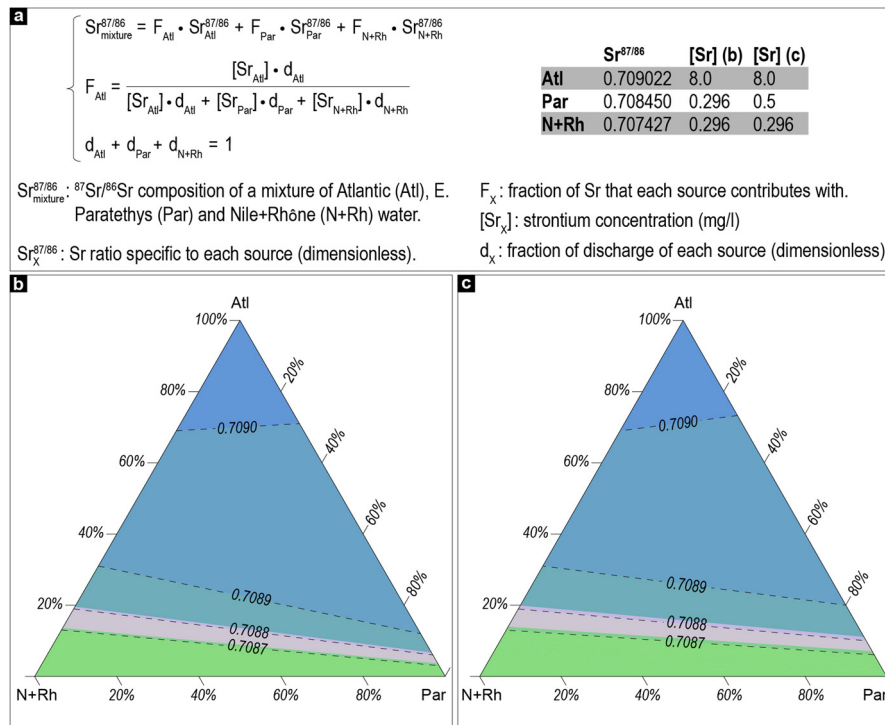**Fig. 5. a:** Mass balance equations and strontium parameter values employed to model the $^{87}Sr/^{86}Sr$ ratio of a water mass mixing Atlantic, Eastern Paratethys and large circum-Mediterranean rivers (Nile and Rhone) waters in various proportions. $^{87}Sr/^{86}Sr_{Atlantic}$ refers to the average value of the range of $^{87}Sr/^{86}Sr$ ratios (0.709017-0.709027) measured on calcareous material assigned to the time interval 5.55 and 5.30 Ma (McArthur et al., 2012). $^{87}Sr/^{86}Sr_{Nile+Rhône}$, $[Sr]_{Atlantic}$ and $[Sr]_{Nile+Rhône}$ are from present-day measurements (e.g. Topper et al., 2011). $^{87}Sr/^{86}Sr_{Paratethys}$ corresponds to the midpoint value of the range of $^{87}Sr/^{86}Sr$ ratios (0.7084-0.7085) derived from ostracods recovered from Stage 3-equivalent sediments in the Caspian Basin (Grothe et al., 2020). **b-c:** Ternary plots of the $^{87}Sr/^{86}Sr$ ratios modeled for a system mixing Atlantic seawater, riverine freshwater from Nile and Rhône and brackish water from the Eastern Paratethys using Two values of $[Sr]_{Paratethys}$, which is the major unknown in the model, are employed. In b, $[Sr]_{Paratethys}$ is 0.296 mg/l, similar to the combination Nile+Rhône, whereas in c the $[Sr]_{Paratethys}$ is slightly higher (0.5 mg/l). The range of $^{87}Sr/^{86}Sr$ ratios measured for the Eraclea Minoa Upper Gypsum layers (pink area) is also plotted to facilitate the comparison with the model outputs. The ternary diagram is generated using the free and open-source software https://www.ternaryplot.com/.
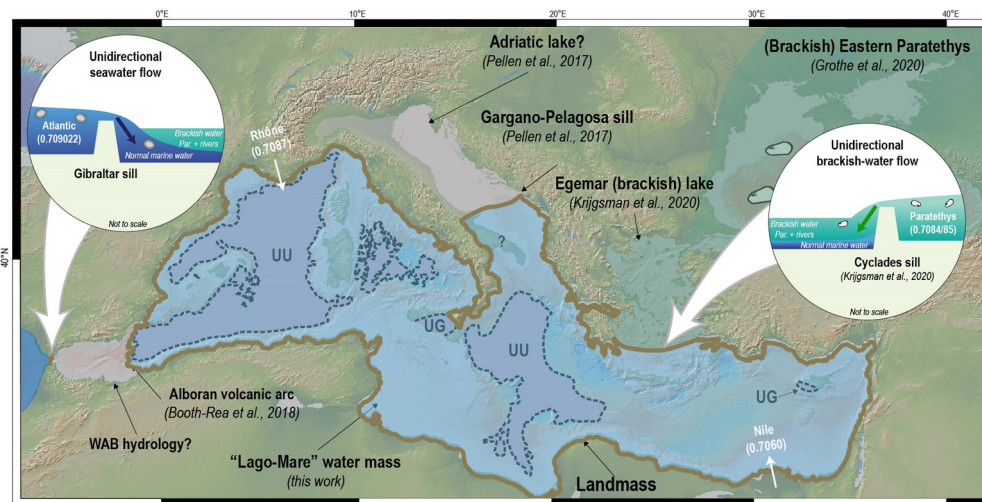

Fig. 6. Snapshot of the Atlantic-Mediterranean-Eastern Paratethys region during times of Stage 3 gypsum precipitation (i.e. sub-units B and C) in Eraclea Minoa. The gypsum-precipitating Lago-Mare water mass is drawn following the present-day spatial distribution of the Upper Gypsum (UG) in the intermediate basins (Sicily and Cyprus) and Upper Unit (UU) in the deep basins (taken from Lofi, 2018). A different water mass was occupying the Stage 3 gypsum-free Northern Aegean, Adriatic and Western Alborán Basin (WAB), likely due to the presence of structural sills. The insets show a schematic close view of the Atlantic-Mediterranean and Mediterranean-Paratethys connections. River water was always draining into the Mediterranean with variable discharge at different moments during a precession/insolation cycle (Simon et al., 2017).

1988; Lugli et al., 2010). Reconstructing base-level changes in ancient evaporitic settings with confidence is difficult because reliable paleobathymetric indicators such as fossils and ichnofossils are commonly absent from high-salinity environments and evaporitic lithofacies are rarely diagnostic of any particular water depth. The UG cycles at Eraclea Minoa are unusual because sub-unit D

contains *in-situ* ostracods which do have paleobathymetric requirements. Living relatives of *C. agrigentina* (e.g. *C. torosa*), which dominates Biofacies 1 (Fig. 2), tolerate only a few tens of meters of water depth (Grossi et al., 2015; Meyer et al., 2016). The more diverse Biofacies 2 at the top of sub-unit D, by contrast, is considered to indicate water depths up to 100 m (Stoica et al., 2016).
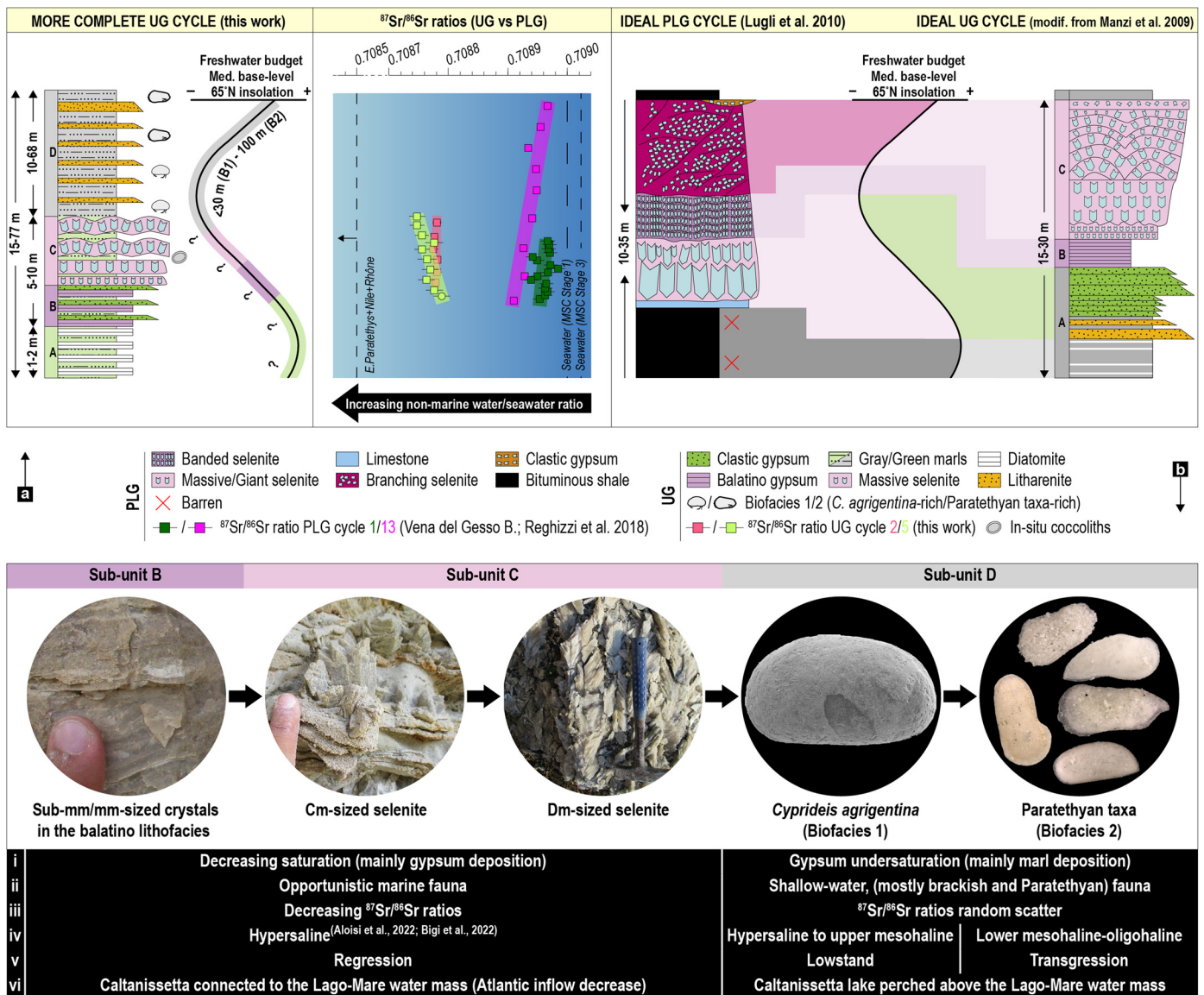
Fig. 7. a: Lithofacies of a complete UG cycle as a function of precession cycle and Mediterranean base-level according to Manzi et al. (2009) and this study. A comparison with the PLG interpretation is also shown (re-drawn after Roveri et al., 2008). The question marks in the figure to the left refer to the uncertainty over the paleodepth during deposition of sub-units A, B and C. Note that our new interpretation of the UG challenges the long-lasting idea that PLG and UG reflect similar depositional mechanisms and paleoenvironmental conditions (Manzi et al., 2009; Roveri et al., 2014a). This is consistent in a number of ways: (1) UG and PLG sequences comprise different facies (UG contains more abundant balatino gypsum and is missing the banded and branching selenite lithofacies of the PLG). (2) Euxinic shales interbedded with the PLG contain possibly in-situ marine fossils (e.g. Corbí and Soria, 2016), whereas the marls interbedded with the UG contain brackish and shallow water ostracods and brackish water foraminifera such as *A. tepida* (Fig. 2; Grossi et al., 2015). This is likely to reflect a greater proportion of marine water in the Mediterranean during Stage 1. (3) $^{87}Sr/^{86}Sr$ isotopes are consistent with the above interpretation, being, on average, close to, or within error of coeval ocean values on stage 1 gypsums (average of 0.708941; Lugli et al., 2010; Reghizzi et al., 2018) and substantially higher than those measured on Stage 3 gypsum samples (average of 0.708752; Fig. 7a). (4) The Stage 3 gypsum $^{87}Sr/^{86}Sr$ data are either constant within the layer or show a subtle decline from base to top (Figs. 5a, 7). This is in contrast with a larger base to top increase in $^{87}Sr/^{86}Sr$ ratio in Stage 1 gypsum layers from the Vena del Gesso Basin (Northern Apennines; Reghizzi et al., 2018; Fig. 7a). (5) The PLG is largely restricted to marginal basins (e.g. Lugli et al., 2010; García-Veigas et al., 2018), whereas the UG is only found in intermediate-deep basins (Fig. 6). **b:** Summary outline of the main sedimentological (i), paleontological (ii) and geochemical (iii) data for each sub-units, their interpretation in terms of salinity (iv) and relationship with the base-level curve (v) and their paleoenvironmental and paleohydrological interpretation proposed in this work (vi).

The ostracod assemblages therefore suggest that the water depth increased during the deposition of sub-unit D (Fig. 7a).

The presence, in one marl layer interbedded with massive selenite beds (sub-unit C) in cycle 3, of both *C. agrigentina* and *L. muelleri*, which is extinct but also thought to have inhabited shallow water (Grossi et al., 2015), suggests that the selenites precipitated in shallow water. However, there is no physical or paleobiological evidence of very shallow water conditions in the cumulate gypsum of sub-unit B. In other ancient evaporitic settings, the transition from cumulates to bottom-grown selenites is commonly interpreted to indicate a shallowing-upward trend (Ortí et

al., 2014; Warren, 2016) and sequences of cumulate and bottom-grown halite layers characterize lake level falls in the Dead Sea today (Sirota et al., 2021). It is possible therefore that the transition from sub-unit B to C equates to a shallowing-upward trend through gypsum deposition (Fig. 7a).

The distribution of gypsum and marl across the Caltanissetta Basin may also provide insights into the relative water depth of the two lithologies. Gypsum occurs throughout the basin with a fairly constant thickness, whereas the evaporite-free marl intervals thin eastward towards the foreland area and above intrabasinal structural highs (Manzi et al., 2009), where they are barren or only

contain Biofacies 1 ostracods (e.g. Balza Soletta section; Maniscalco et al., 2019). Manzi et al. (2009) interpreted this distribution as the consequence of continuous subaqueous deposition with eastward thinning of the marls related to increased distance from the terrigenous source. An alternative interpretation is that the base-level was high enough to precipitate gypsum across the whole Caltanissetta Basin, but dropped during marl deposition, exposing more marginal areas to erosion and/or non-deposition and leaving only the deeper depocenters (e.g. Eraclea Minoa) underwater. During the subsequent base-level rise, recorded in Eraclea Minoa by the appearance of Biofacies 2 ostracods, these marginal areas were drowned again and accumulated thin, Biofacies 1-bearing marls. If correct, this interpretation suggests that there was a higher water level at the beginning of gypsum precipitation than at the beginning of sub-unit D marls (Fig. 7a).

If the Caltanissetta Basin was part of a larger Lago-Mare water mass, cyclical base-level changes seen there are likely to be the consequence of fluctuations in the discharge of one, or more, of the Mediterranean's water sources. The Mediterranean's freshwater budget is highly variable on precession timescales. It is enhanced during the insolation maxima, when more rainwater from North African monsoon and Atlantic storms is delivered to the Mediterranean (e.g. Marzocchi et al., 2016), and it reaches the lowest values during the insolation minima, when less freshwater is supplied and more water is lost by evaporation. It is therefore likely that base-level variations were in phase with the insolation forcing: the highstands coincided with insolation maxima and the lowstands with insolation minima (e.g. Simon et al., 2017). Previously, the gypsum beds at Eraclea Minoa have been correlated with increasing insolation following the insolation minima and the diatomites and ostracod-bearing marls tied to the transition from insolation maxima to minima (Fig. 7a; van der Laan et al., 2006; Manzi et al., 2009). This is challenged by the relative base-level changes reconstructed here, which instead suggest that the base of the ostracod-bearing marls at Eraclea Minoa represents lowstand phases, corresponding to insolation minima (Fig. 7a), while the shallowing through gypsum sub-units B and C, corresponds to part of the transition from insolation maxima to minima (Fig. 7a).

This revised astronomical tuning dates the base of the Upper Gypsum at Eraclea Minoa to ∼5.515 Ma and the first indication of Paratethyan ostracods to ∼5.47 Ma. This is the oldest age known in the Mediterranean and contradicts the hypothesis that the migration of Paratethyan ostracods occurred as a single Mediterranean-wide event at 5.42 Ma (substages 3.1 and 3.2 (or Lago-Mare phase) of Roveri et al., 2014a; see also Roveri et al., 2008 and Grossi et al., 2011), possibly prompted by a sudden increase of the Paratethys outflow (Marzocchi et al., 2016).

4.4. Connectivity changes terminated gypsum precipitation

The UG sediments at Eraclea Minoa also contain evidence of changing palaeoenvironmental conditions. The vertical transition from sub-mm/mm-sized gypsum crystals in the balatino lithofacies (sub-unit B), which require supersaturated conditions favoring the formation of new nuclei over crystal growth (Lugli et al., 2010), to increasingly larger selenites (sub-unit C), which require gradually lower degree of brine supersaturation to grow larger (Lugli et al., 2010), is indicative of a progressive reduction of the brine concentration approaching the transition with sub-unit D. Then, the sub-unit C/D transition marks a major paleoenvironmental and paleohydrological event, testified by the abrupt cessation of gypsum precipitation and the appearance of shallow-water fauna. Microthermometry studies on fluid inclusions in gypsum lithofacies (Bigi et al., 2022) and thermodynamic calculations (Aloisi et al., 2022) show that the Eraclea gypsums precipitated from the evaporation of seawater at a salinity ∼ 115 g kg^{-1}. The ostracods in

the overlying marls show a gradual transition from dominantly *C. agrigentina* (Biofacies 1), which tolerates a wide range of salinities (Grossi et al., 2015), to the more diverse Biofacies 2, which indicate fresher (oligohaline) conditions (Fig. 7b; Stoica et al., 2016).

One possibility is that the gradual drop in concentration with respect to gypsum and the salinity decrease across the sub-unit C/D transition and through sub-unit D were prompted by increased continental runoff (Manzi et al., 2009). In this case, however, a base-level rise should have accompanied the precipitation of gypsum, in order to bring enough ions for it to precipitate. In turn, this means that the base level would reach the highstand during deposition of Biofacies 2 (Fig. 7a; Manzi et al., 2009). This scenario is in contradiction with our water level reconstruction, that indicate a shallowing through the gypsum and a deepening through the sub-unit D marls (Fig. 7a). The lessening of Atlantic inflow, which achieves both the base-level fall through sub-units B-C and the associated subtle declining trend in the ^{87}Sr/^{86}Sr ratios within individual gypsums (Figs. 2, 7a), seems to be a more plausible mechanism. In the context of deposition during a Mediterranean base-level fall, it is possible, therefore, that the abrupt transition from gypsum to ostracod-bearing marls was the consequence of the base level falling below the Caltanissetta Basin, leaving it as a perched lacustrine system above the deeper areas covered by the "Lago-Mare" water mass. The generally lower ^{87}Sr/^{86}Sr ratios and larger ^{87}Sr/^{86}Sr variations in the Eraclea Minoa marls, indicate a greater influence of freshwater inputs to the basin compared to the gypsums that have higher and less variable ^{87}Sr/^{86}Sr ratios. This suggests that the Caltanissetta Basin formed a perched lake during marl deposition at lowstands. Compared to seawater-influenced basins, lacustrine settings are, indeed, much more sensitive to subtle changes in fluvial discharge (e.g. Bista et al., 2021), resulting in rapid changes in the ^{87}Sr/^{86}Sr ratio measured on the ostracods.

4.5. High amplitude fluctuations of the Mediterranean base-level

The same ostracods biofacies as those in sub-unit D are found both in marginal Mediterranean marls, where they typically alternate with continental facies, and in the deep basins (e.g. Sites 975B, 372, 129A; see Andreetto et al., 2021a), where the marls alternate with laminated and clastic gypsum (Andreetto et al., 2021a). For the deep basins to develop the shallow-water conditions required by the ostracods, the Mediterranean water level had to fall below the intermediate position of the Caltanissetta Basin. This means that Caltanissetta and deeper basins accumulated the shallow-water ostracod-bearing marls during lowstand phases of the Lago-Mare water, exposing the marginal basins to continental deposition and/or erosion (Fig. 8e). By contrast, higher Mediterranean water levels are required to populate the shallow marginal basins with these same Paratethyan ostracods (Stoica et al., 2016). This is supported by the ^{87}Sr/^{86}Sr ratios measured on some of these marginal basin ostracods, which point to mixing between high-^{87}Sr/^{86}Sr local fluvial waters with the Lago-Mare water mass (Andreetto et al., 2021b, 2022). During these highstand phases of marginal basin ostracod-rich marl deposition, the Caltanissetta and deep basins were experiencing much deeper water conditions (i.e. several hundreds of meters; Fig. 8b).

The depth constraints provided by the shallow-water ostracod assemblages indicate that marl deposition was not synchronous across the Mediterranean during base-level highstands at insolation maxima (Roveri et al., 2008, 2014a), but sequential, tracking Mediterranean-wide, high-amplitude (several hundred to thousands of meters) base-level fluctuations (Figs. 8b-e). This model of high-amplitude base level changes, earlier hypothesized by Hardie and Lowenstein (2004) and Rouchy and Caruso (2006) is now supported by integrated sedimentological, paleontological and geochemical observations that show that the Mediterranean was at
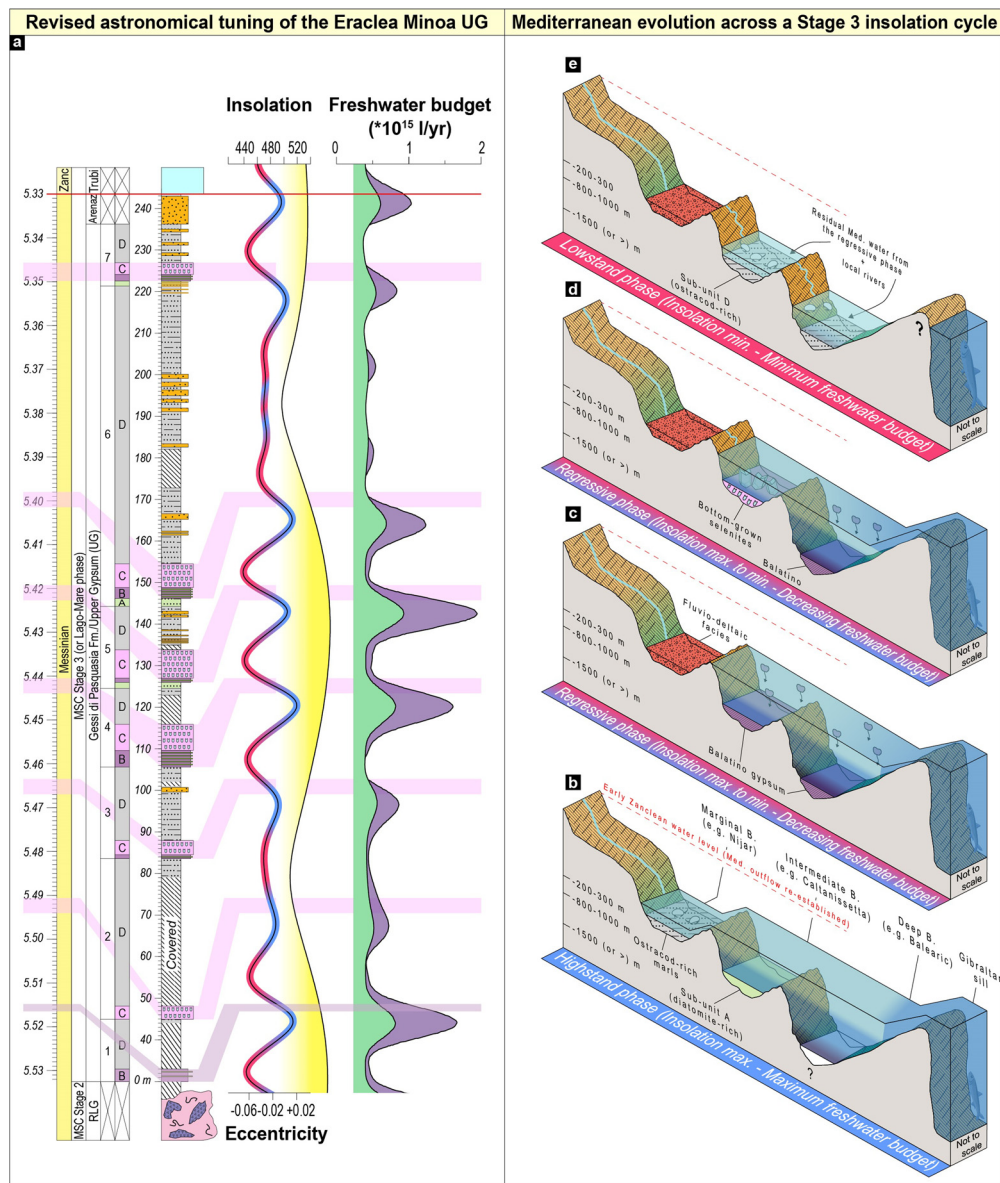
Fig. 8. a: Revised astronomical tuning of the Upper Gypsum Unit at Eraclea Minoa according to the newly proposed phase relationships between the UG lithofacies and the astronomical forcing (namely 65°N summer insolation and 100 kyr eccentricity curves). Starting from the conformable M/P boundary, we correlate the seven gypsum beds to successive transitions from insolation maxima to minima avoiding the insolation peaks associated with the 100-kyr eccentricity minima at ∼5.38 Ma and ∼5.50 Ma. Due to the low amplitude of insolation in these eccentricity low, these minor peaks are not expected to correspond to a gypsum bed in the sedimentary record (van der Laan et al., 2006). It is more likely that these low eccentricities corresponded to prolonged phases of very low base level in the Mediterranean (Fig. 8a). Pursuing this approach, all gypsum beds follow well pronounced insolation maxima and the thicker, gypsum-free, *Cyprideis*-rich sub-units D between gypsums II-III and VI-VII correlate with an eccentricity minimum. The overall Mediterranean run-off budget from Simon et al. (2017), with included (violet curve) and excluded (green curve) supply from the Chad lake, is also shown. **b-e**: Cartoons showing the proposed evolution of the Mediterranean environments and hydrology during one precession cycle of MSC Stage 3.

times both relatively full (Fig. 8b) and empty (Fig. 8e) during each Stage 3 precession cycle. This model helps reconcile observations that support the full versus desiccated debate that has afflicted the MSC Stage 3 successions for decades (Andreetto et al., 2021a).

4.6. Implications of Atlantic-Mediterranean connectivity for ocean chemistry

On long timescales (>100 kyr), marine alkalinity and CaCO$_3$ burial are balanced by the response of silicate weathering to changes in atmospheric CO$_2$ and associated temperature. Many biogeochemical models (e.g. Berner, 1991; Lenton et al., 2018) assume that on these long timescales perturbations to seawater chemistry caused by evaporite precipitation are balanced by evaporite dissolution during weathering. However, evaporites form

and dissolve three orders of magnitude more quickly than other sediments (Nichols et al., 2009) and this approach fails to consider whether abrupt and short-term evaporite-driven chemical perturbations can propagate into aspects of the carbon cycle that have longer-term climate implications. The box model study by Shields and Mills (2020) explores the impact of gypsum on ocean chemistry and its knock-on consequences for CaCO$_3$ burial, atmospheric CO$_2$ and global temperature by allowing the non-steady-state ocean calcium inventory to be driven by CaSO$_4$ precipitation and the return flux to the ocean from weathering. Their results demonstrate that a decrease in ocean [Ca] as a consequence of gypsum deposition, because it is not associated with an alkalinity change, leads to decreasing CaCO$_3$ burial and higher oceanic pH, resulting in decreasing atmospheric CO$_2$ and global cooling (Shields and Mills, 2020). However, their sensitivity experiments

impose a constant gypsum precipitation and weathering forcing for 1 million years which is not a realistic reflection of the pattern of ocean [Ca] extraction as a consequence of the MSC. Here we explore what a realistic evaporite precipitation and weathering flux would look like over the duration of the MSC and consider its possible implications.

In contrast with the constant precipitation driver modeled by Shields and Mills (2020), the precessional gypsum-marl cyclicity that characterizes both MSC Stage 1 and 3 suggests that extraction of Ca^{2+} and SO_4^{2-} ions from the global ocean was episodic and probably endured for only a few thousand years in each precession cycle. Further modeling experiments are required to evaluate the degree to which the regular switching on and off of gypsum precipitation modifies the modeled consequences for carbonate burial, atmospheric CO_2 and global temperatures (Shields and Mills, 2020) as a result of (partial) recovery of the system between evaporite pulses. However, without near synchronous return of Ca^{2+} ions to the ocean as a result of evaporite weathering, the reduction in oceanic [Ca] is unlikely to have bounced back completely, leading to a progressive decline in seawater [Ca] from one precessional evaporite event to the next. Stage 2 evaporites are heavily dominated by halite, not gypsum. However, it is possible that constant extraction of these Ca^{2+} ions did characterize the $\sim$50 kyr duration of this phase of the MSC, since the volumetrics of the halite succession preserved, requires constant input of ocean water (Krijgsman and Meijer, 2008) which must also have contained Ca^{2+} and SO_4^{2-}. Taken together then, the rate of Ca^{2+} ion extraction over the course of the entire MSC is likely to have varied and to have been most substantial during Stage 2.

Recent evaporite volume estimates for the MSC (Haq et al., 2020) are broadly similar to those used by Shields and Mills (2020) to estimate the scale of the Ca^{2+} extraction during salt giant formation. Both are based on the volumes of evaporites that are still preserved in the Mediterranean today, and therefore represent a minimum. That being the case, whether pulsed or continuous, this Late Miocene episode of $CaSO_4$ extraction may have contributed to the cooling seen in time-equivalent SST records (Herbert et al., 2016).

Although the net effect of the MSC was to extract Ca^{2+} and SO_4^{2-} from the global ocean, the episodic nature of gypsum accumulation and Mediterranean-Atlantic connectivity also implies that the Mediterranean was, intermittently and at time-scales shorter than the MSC, a net source of Ca^{2+} and SO_4^{2-} to the Atlantic. Evaluating episodic net Ca^{2+} and SO_4^{2-} fluxes to the ocean during the MSC is particularly challenging since it depends not on the gypsum preserved today in the Mediterranean, but rather on what was originally precipitated and has been already dissolved (Wortmann and Payton, 2012). However, what we can evaluate from the Mediterranean's geological record is the nature of its connectivity with the Atlantic and from this it is possible to deduce the timing and likely duration of episodic net exchange of Ca^{2+} and SO_4^{2-} between the Mediterranean to the global ocean.

Evidence from both $^{87}Sr/^{86}Sr$ data and box-modeling indicate that Stage 1 gypsum was precipitated while the Mediterranean experienced restricted, but two-way exchange with the Atlantic under conditions which broadly maintained eustatic sea level in the Mediterranean (e.g. Flecker et al., 2015 and references therein). This configuration will have resulted in net extraction of Ca^{2+} and SO_4^{2-} ions from the ocean, at least during gypsum precipitation. Maximum dissolution of gypsum occurs during subaerial exposure with the formation of aquifers associated with active hydrology (Gustavson et al., 1982). Since there is no evidence of substantial base-level fall during the marl intervals in Stage 1, it is probable that there was relatively little weathering of the gypsum and therefore a limited return flux of these ions to the ocean.

The connectivity and base-level configurations during stages 2 and 3 are substantially different. Outflow to the Atlantic ceased, base-level fell and then, as shown in this study, fluctuated substantially during Stage 3. This exposed the Stage 1 gypsum that precipitated on the margins and stage 2 and 3 gypsum reworked or precipitated in deeper settings of the Mediterranean, to dissolution. However, without Mediterranean outflow, these weathered evaporitic ions were trapped in the Mediterranean and had no influence on global ocean chemistry. Outflow to the Atlantic started abruptly at the beginning of the Pliocene with the termination of the MSC, triggering the return of two-way exchange and the reestablishment of open marine conditions in the Mediterranean.

In summary, the MSC evaporite weathering flux to the ocean was episodic and largely out of phase with gypsum precipitation-driven extraction, potentially resulting in dynamic changes to ocean chemistry on the timescale of the MSC. Interestingly, the main impact Shields and Mills (2020) found of modeling a 1 million year $CaSO_4$ weathering event was a rapid rise in $CaCO_3$ burial and a transient peak in atmospheric CO_2 concentration and associated warming, that occurred only 150 kyrs after initiation. With this in mind, it is tempting to attribute at least part of the abrupt warming in early Pliocene sea surface temperature records (Herbert et al., 2016) to a Mediterranean-derived pulse of Ca^{2+} ions. Testing this hypothesis will require more sophisticated biogeochemical modeling and better quantitative constraints on the chemistry of Mediterranean outflow. If true however, it would suggest that the most important impact of the Zanclean deluge was not the sudden inundation of a Mediterranean empty of water for hundreds of thousands of years, but the abrupt flushing into the Atlantic of the ponded brine and weathering products of a salt giant.

5. Conclusions

The UG selenites at Eraclea Minoa contain in-situ marine calcareous nannofossils and display $^{87}Sr/^{86}Sr$ ratios which indicate that a small Atlantic flux ($\leq$20%) supplied the Mediterranean with Ca^{2+} and SO_4^{2-} ions during gypsum precipitation. Mass-balance calculations suggest that the remaining $\geq$80% of the Lago-Mare water mass was supplied by Eastern Paratethys and large Mediterranean rivers. Gypsum precipitation, first from settling crystals nucleated in the water column (balatino, sub-unit B) and then from bottom-grown selenites (sub-unit C), occurred during a phase of base-level fall coincident with the transition from insolation maxima to insolation minima. During insolation minima, low diversity ostracod-bearing marls (Biofacies 1 of sub-unit D), that constrain the water depth to a few tens of meters, were deposited in an isolated, lacustrine Caltanissetta Basin perched above the Lago-Mare water mass, which persisted in the deep subbasins. The transition from Biofacies 1 to 2 indicates rising water levels in the lake. Similar ostracod-bearing marls are found in both shallower and deeper settings across the Mediterranean, indicating that marl deposition was asynchronous during Stage 3, tracking high-amplitude, Mediterranean-wide base level changes (Fig. 8a). Sedimentological, geochemical and biological data from Eraclea Minoa suggest that the Mediterranean experienced (at least) 7 substantial, cyclic base-level changes during Stage 3. A revised astronomical tuning indicates that MSC Stage 3 started at 5.515 Ma, with the first occurrence of Paratethyan ostracods on Sicily at 5.47 Ma. This model for (upper) gypsum formation, which envisages periods during which the Mediterranean was both relatively full and empty, helps to reconcile many of the discrepancies between offshore- and onshore-based interpretations of the final phase of the Messinian Salinity Crisis. It also suggests that any impact of the Mediterranean salt giant formation and evaporite weathering during stages

2 and/or 3 on ocean biogeochemistry occurred in the Pliocene once Mediterranean outflow was re-established.

CRediT authorship contribution statement

Declaration of competing interest

The authors declare that they have no known competing financial interests or personal relationships that could have appeared to influence the work reported in this paper.

Data availability

All data used for the research are present in the article.

Acknowledgements

References

Aloisi, G., Guibourdenche, L., Natalicchio, M., Caruso, A., Haffert, L., El Kilany, A., Pierre, F.D., 2022. The geochemical riddle of "low-salinity gypsum" deposits. Geochim. Cosmochim. Acta 327, 247–275. https://doi.org/10.1016/j.gca.2022.03.033.

Andreetto, F., Aloisi, G., Raad, F., Heida, H., Flecker, R., Agiadi, K., Lofi, J., Blondel, S., Bulian, F., Camerlenghi, A., Caruso, A., Ebner, R., Garcia-Castellanos, D., Gaullier, V., Guibourdenche, L., Gvirtzman, Z., Hoyle, T.M., Meijer, P.T., Moneron, J., Sierro, F.J., Travan, G., Tzevahirtzian, A., Vasiliev, I., Krijgsman, W., 2021a. Freshening of the Mediterranean Salt Giant: controversies and certainties around the terminal (Upper Gypsum and Lago-Mare) phases of the Messinian salinity crisis. Earth-Sci. Rev. 216, 1–47. https://doi.org/10.1016/j.earscirev.2021.103577.

Andreetto, F., Matsubara, K., Beets, C.J., Fortuin, A.R., Flecker, R., Krijgsman, W., 2021b. High Mediterranean water-level during the Lago-Mare phase of the Messinian Salinity Crisis: insights from the Sr isotope records of Spanish marginal basins (SE Spain). Palaeogeogr. Palaeoclimatol. Palaeoecol. 562. https://doi.org/10.1016/j.palaeo.2020.110139.

Andreetto, F., Mancini, A.M., Flecker, R., Gennari, R., Lewis, J., Lozar, F., Natalicchio, M., Sangiorgi, F., Stoica, M., Dela Pierre, F., Krijgsman, W., 2022. Multi-proxy investigation of the post-evaporitic succession of the Piedmont Basin (Pollenzo section, NW Italy): a new piece in the Stage 3 puzzle of the Messinian Salinity Crisis. Palaeogeogr. Palaeoclimatol. Palaeoecol., 110961. https://doi.org/10.1016/j.palaeo.2022.110961.

Auer, G., Piller, W.E., Mathias Harzhauser, M., 2014. High-resolution calcareous nannoplankton paleoecology as a proxy for small-scale environmental changes in the Early Miocene. Mar. Micropaleontol. 111, 53–65. https://doi.org/10.1016/j.marmicro.2014.06.005.

Berner, R.A., 1991. A model for atmospheric CO sub 2 over Phanerozoic time. Am. J. Sci. 291 (4).

Bigi, D., Lugli, S., Manzi, V., Roveri, M., 2022. Are fluid inclusions in gypsum reliable paleoenvironmental indicators? An assessment of the evidence from the Messinian evaporites. Geology 50, 454–459. https://doi.org/10.1130/G49475.1.

Bista, D., Hoyle, T.M., Simon, D., Sangiorgi, F., Richards, D.A., Flecker, R., 2021. Sr isotope-salinity modelling constraints on Quaternary Black Sea connectivity. Quat. Sci. Rev. 273, 107254. https://doi.org/10.1016/j.quascirev.2021.107254.

Blanc-Valleron, M.-M., Rouchy, J.-M., Pierre, C., Badaut-Trauth, D., Schuler, M., 1998. Evidence of Messinian nonmarine deposition at site 968 (Cyprus lower slope). In: Proceedings of the Ocean Drilling Program, Scientific Results. ODP Sci. Results 160. Texas, USA, pp. 43–445.

Booth-Rea, G., Ranero, R., Grevemeyer, I.C., 2018. The Alboran volcanic-arc modulated the Messinian faunal exchange and salinity crisis. Sci. Rep. 8. https://doi.org/10.1038/s41598-018-31307-7.

Caruso, A., Rouchy, J.M., 2006. The Upper Gypsum unit. In: Roveri, M. (Ed.), Post-Congress FieldTrip of the RCMNS Interim Colloquium. Parma, 2006. In: Acta Naturalia de "L'Ateneo Parmense", vol. 42, pp. 157–168.

Flecker, R., Krijgsman, W., Capella, W., de Castro Martíns, C., Dmitrieva, E., Mayser, J.P., Marzocchi, A., Modestu, S., Ochoa, D., Simon, D., Tulbure, M., van den Berg, B., van der Schee, M., de Lange, G., Ellam, R., Govers, R., Gutjahr, M., Hilgen, F., Kouwenhoven, T., Lofi, J., Meijer, P., Sierro, F.J., Bachiri, N., Barhoun, N., Alami, A.C., Chacon, B., Flores, J.A., Gregory, J., Howard, J., Lunt, D., Ochoa, M., Pancost, R., Vincent, S., Yousfi, M.Z., 2015. Evolution of the late Miocene Mediterranean-Atlantic gateways and their impact on regional and global environmental change. Earth-Sci. Rev. 150, 365–392. https://doi.org/10.1016/j.earscirev.2015.08.007.

García-Veigas, J., Cendón, D.I., Gibert, L., Lowenstein, T.K., Artiaga, D., 2018. Geochemical indicators in Western Mediterranean Messinian evaporites: Implications for the salinity crisis. Mar. Geol. 403, 197–214. https://doi.org/10.1016/j.margeo.2018.06.005.

Griffin, D., 2006. The late Neogene Sahabi rivers of the Sahara and their climatic and environmental implications for the Chad basin. J. Geol. Soc. 163, 905–921.

Grossi, F., Gliozzi, E., Cosentino, D., 2011. Parathethyan ostracod immigrants mark the biostratigraphy of the Messinian Salinity Crisis. In: 7th European Ostracodologist's Meeting. Graz, 25-28 July, 2011. In: Joannea Geologie und Palaeontologie, vol. 11, pp. 66–68.

Grossi, F., Gliozzi, E., Anadón, P., Castorina, F., Voltaggio, M., 2015. Is Cyprideis agrigentina Decima a good paleosalinometer for the Messinian Salinity Crisis? Morphometrical and geochemical analyses from the Eraclea Minoa section (Sicily). Palaeogeogr. Palaeoclimatol. Palaeoecol. 419, 75–89. https://doi.org/10.1016/j.paleo.2014.09.024.

Grothe, A., Andreetto, F., Reichart, G.J., Wolthers, M., Van Baak, C.G., Vasiliev, I., Stoica, M., Sangiorgi, F., Middelburg, J.J., Davies, G.R., Krijgsman, W., 2020. Parathethys pacing of the Messinian Salinity Crisis: low salinity waters contributing to gypsum precipitation? Earth Planet. Sci. Lett. 532, 116029. https://doi.org/10.1016/j.epsl.2019.116029.

Gustavson, T.C., Smpkins, W.W., Alhades, A., Hoadley, A., 1982. Evaporite dissolution and development of karst features on the Rolling Plains of the Texas Panhandle. Earth Surf. Process. Landf. 7 (6), 545–563.

Haq, B., Gorini, C., Baur, J., Moneron, J., Rubino, J.L., 2020. Deep Mediterranean's Messinian evaporite giant: how much salt? Glob. Planet. Change 184, 103052. https://doi.org/10.1016/j.gloplacha.2019.103052.

Hardie, L.A., Lowenstein, T.K., 2004. Did the Mediterranean Sea dry out during the Miocene? A reassessment of the evaporite evidence from DSDP Legs 13 and 42A cores. J. Sediment. Res. 74, 453–461.

Herbert, T.D., Lawrence, K.T., Tzanova, A., Peterson, L.C., Caballero-Gill, R., Kelly, C.S., 2016. Late Miocene global cooling and the rise of modern ecosystems. Nat. Geosci. 9 (11), 843–847. https://doi.org/10.1038/ngeo2813.

Keogh, S.M., Butler, R.W.H., 1999. The Mediterranean water body in the late Messinian: interpreting the record from marginal basins on Sicily. J. Geol. Soc. 156 (4), 837–846.

Krijgsman, W., Meijer, P.T., 2008. Depositional environments of the Mediterranean "Lower Evaporites" of the Messinian salinity crisis: constraints from quantitative analyses. Mar. Geol. 253 (3–4), 73–81. https://doi.org/10.1016/j.margeo.2008.04.010.

Krijgsman, W., Capella, W., Simon, D., Hilgen, F.J., Kouwenhoven, T.J., Meijer, P.Th., Sierro, F.J., Tulbure, M.A., van den Berg, B.C.J., van der Schee, M., Flecker, R., 2018. The Gibraltar Corridor: watergate of the Messinian Salinity Crisis. Mar. Geol. 403, 238–246. https://doi.org/10.1016/j.margeo.2018.06.008.

Krijgsman, W., Palcu, D., Andreetto, F., Stoica, M., Mandic, O., 2020. Changing seas in the late Miocene Northern Aegean: a Paratethyan approach to Mediterranean basin evolution. Earth-Sci. Rev. 103386. https://doi.org/10.1016/j.earscirev.2020.103386.

Lenton, T.M., Daines, S.J., Mills, B.J., 2018. COPSE reloaded: an improved model of biogeochemical cycling over Phanerozoic time. Earth-Sci. Rev. 178, 1–28. https://doi.org/10.1016/j.earscirev.2017.12.004.

Lofi, J., 2018. Seismic Atlas of the Messinian salinity crisis markers in the Mediterranean sea. Volume 2 - M´emoires de la Société géologique de France, n.s., 2018, t. 181, and Commission for the Geological Map of the World, 72 p. + DVD. https://doi.org/10.10682/2018M ESSINV2.

Lowenstein, T.K., 1988. Origin of depositional cycles in a Permian "saline giant": the Salado (McNutt zone) evaporites of New Mexico and Texas. Geol. Soc. Am. Bull. 100 (4), 592–608.

Lugli, S., Manzi, V., Roveri, M., Schreiber, B.C., 2010. The Primary Lower Gypsum in the Mediterranean: a newfacies interpretation for the first stage of the Messinian salinity crisis. Palaeogeogr. Palaeoclimatol. Palaeoecol. 297, 83–99. https://doi.org/10.1016/j.paleo.2010.07.017.

Maniscalco, R., Casciano, C.I., Distefano, S., Grossi, F., Di Stefano, A., 2019. Facies analysis in the Second Cycle Messinian evaporites predating the early Pliocene reflooding: the Balza Soletta section (Corvillo Basin, central Sicily). Ital. J. Geosci. 138 (3), 301–316. https://doi.org/10.3301/IJG.2019.06.

Manzi, V., Lugli, S., Roveri, M., Schreiber, B.C., 2009. A new facies model for the Upper Gypsum of Sicily (Italy): chronological and paleoenvironmental constraints for the Messinian salinity crisis in the Mediterranean. Sedimentology 56, 1937–1960. https://doi.org/10.1111/j.1365-3091.2009.01063.x.

Manzi, V., Roveri, M., Argnani, A., Cowan, D., Lugli, S., 2021. Large-scale mass-transport deposits recording the collapse of an evaporitic platform during the Messinian salinity crisis (Caltanissetta basin, Sicily). Sediment. Geol. 424, 106003. https://doi.org/10.1016/j.sedgeo.2021.106003.

Marzocchi, A., Flecker, R., Van Baak, C.G.C., Lunt, D.J., Krijgsman, W., 2016. Mediterranean outflow pump: an alternative mechanism for the Lago-mare and the end of the Messinian Salinity Crisis. Geology 44, 523–526. https://doi.org/10.1130/G37646.

McArthur, J.M., Howarth, R.J., Shields, G.A., 2012. Strontium isotope stratigraphy. In: Gradstein, F.M., Ogg, J.G., Schmitz, M.D., Ogg, G.M. (Eds.), The Geological Time Scale 2012. Elsevier B.V., Oxford, pp. 127–144.

Meyer, J., Wrozyna, C., Gross, M., Leis, A., Piller, W.E., 2016. Morphological and geochemical variations of Cyprideis (Ostracoda) from modern waters of the northern Neotropics. Limnology, first published online October 6, 2016. https://doi.org/10.1007/s10201-016-0504-9.

Müller, D.W., Mueller, P.A., McKenzie, J.A., 1990. Strontium Isotopic Ratios as Fluid Tracers in Messinian Evaporites of the Tyrrhenian Sea (Western Mediterranean Sea). Proceedings of the Ocean Drilling Program, Scientific Results, vol. 107. Ocean Drill. Program, College Station, Tex, pp. 603–614.

Nichols, G., Williams, E., Paola, C. (Eds.), 2009. Sedimentary Processes, Environments and Basins: A Tribute to Peter Friend. John Wiley & Sons.

Ortí, F., Rosell, L., Gibert, L., Moragas, M., Playà, E., Inglès, M., Rouchy, J.M., Calvo, P.J., Gimeno, D., 2014. Evaporite sedimentation in a tectonically active basin: the lacustrine Las Minas Gypsum unit (Late Tortonian, SE Spain). Sediment. Geol. 311, 17–42. https://doi.org/10.1016/j.sedgeo.2014.06.004.

Pellegrino, L., Natalicchio, M., Abe, K., Jordan, R.W., Longo, S.E.F., Ferrando, S., Carnevale, G., Dela Pierre, F., 2021. Tiny, glassy, and rapidly trapped: the nano-sized planktic diatoms in Messinian (late Miocene) gypsum. Geology 49 (11), 1369–1374. https://doi.org/10.1130/G49342.1.

Pellen, R., Popescu, S.-M., Suc, J.-P., Melinte-Dobrinescu, M.C., Rubino, J.-L., Rabineau, M., Marabini, S., Loget, N., Casero, P., Cavazza, W., Head, M.J., Aslanian, D., 2017. The Apennine foredeep (Italy) during the latest Messinian: Lago Mare reflects competing brackish and marine conditions based on calcareous nannofossils and dinoflagellate cysts. Geobios 50, 237–257. https://doi.org/10.1016/j.geobios.2017.04.004.

Pierre, C., Rouchy, J.M., 1990. Stable isotope composition of carbonates in the Tyrrhenian Sea. PANGAEA. Sulement to: Pierre, C; Rouchy, JM (1990): Sedimentary and diagenetic evolution of Messinian evaporites in the Tyrrhenian Sea (ODP Leg 107, Sites 652, 653, and 654): petrographic, mineralogical, and stable isotope records. In: Kastens, KA; Mascle, J; et al. (eds.), Proceedings of the Ocean Drilling Program, Scientific Results, College Station, TX (Ocean Drilling Program), 107, 187-210. https://doi.org/10.2973/odp.proc.sr.107.131.1990.

Raad, F., Lofi, J., Maillard, A., Tzevahirtzian, A., Caruso, A., 2021. The Messinian Salinity Crisis deposits in the Balearic Promontory: an undeformed analog of the MSC Sicilian basins? Mar. Pet. Geol., 104777. https://doi.org/10.1016/j.marpetgeo.2020.104777.

Reghizzi, M., Lugli, S., Manzi, V., Rossi, F.P., Roveri, M., 2018. Orbitally forced hydrological balance during the Messinian Salinity Crisis: insights from Strontium Isotopes ($^{87}Sr/^{86}Sr$) in the Vena del Gesso Basin (Northern Apennines, Italy). Paleoceanogr. Paleoclimatol. 33 (7), 716–731. https://doi.org/10.1029/2018PA003395.

Rouchy, J.M., Caruso, A., 2006. The Messinian salinity crisis in the Mediterranean basin: a reassessment of the data and an integrated scenario. Sediment. Geol. 188, 35–67. https://doi.org/10.1016/j.sedgeo.2006.02.005.

Roveri, M., Lugli, S., Manzi, V., Schreiber, B.C., 2008. The Messinian salinity crisis: a sequence-stratigraphic approach. GeoActa 1, 169–190.

Roveri, M., Flecker, R., Krijgsman, W., Lofi, J., Lugli, S., Manzi, V., Sierro, F.J., Bertini, A., Camerlenghi, A., De Lange, G., Govers, R., Hilgen, F.J., Hübscher, C., Meijer, P.Th., Stoica, M., 2014a. The Messinian salinity crisis: past and future of a great challenge for marine sciences. Mar. Geol. 349, 113–125. https://doi.org/10.1016/j.margeo.2014.02.002.

Roveri, M., Lugli, S., Manzi, V., Gennari, R., Schreiber, B.C., 2014b. High resolution strontium isotope stratigraphy of the Messinian deep Mediterranean basins: implications for marginal to central basins correlation. Mar. Geol. 349, 113–125. https://doi.org/10.1016/j.margeo.2014.01.002.

Shields, G.A., Mills, B.J.W., 2020. Evaporite weathering and deposition as a long-term climate forcing mechanism. Geology 49, 299–303. https://doi.org/10.1130/G48146.1.

Simon, D., Marzocchi, A., Flecker, R., Lunt, D.J., Hilgen, F.J., Meijer, P.T., 2017. Quantifying the Mediterranean freshwater budget throughout the late Miocene: new implications for sapropel formation and the Messinian Salinity Crisis. Earth Planet. Sci. Lett. 472, 25–37. https://doi.org/10.1016/j.epsl.2017.05.013.

Sirota, I., Enzel, Y., Mor, Z., Ben Moshe, L., Eyal, H., Lowenstein, T.K., Lensky, N.G., 2021. Sedimentology and stratigraphy of a modern halite sequence formed under Dead Sea level fall. Sedimentology 68 (3), 1069–1090. https://doi.org/10.1111/sed.12814.

Stoica, M., Krijgsman, W., Fortuin, A., Gliozzi, E., 2016. Parathethyan ostracods in the Spanish Lago-Mare: more evidence for inter-basinal exchange at high Mediterranean sea level. Palaeogeogr. Palaeoclimatol. Palaeoecol. 441, 854–870. https://doi.org/10.1016/j.paleo.2015.10.034.

Topper, R.P.M., Flecker, R., Meijer, P.T., Wortel, M.J.R., 2011. A box model of the Late Miocene Mediterranean Sea: implications from combined 87Sr/86Sr and salinity data. Paleoceanography 26, PA3223. https://doi.org/10.1029/2010PA002063.

Topper, R.P.M., Lugli, S., Manzi, V., Roveri, M., Meijer, P.T., 2014. Precessional control of Sr ratios in marginal basins during the Messinian salinity crisis? Geochem. Geophys. Geosyst. 15 (5), 1926–1944. https://doi.org/10.1002/2013GC005192.

van der Laan, E., Snel, E., de Kaenel, E., Hilgen, F.J., Krijgsman, W., 2006. No major deglaciation across the Miocene-Pliocene boundary: integrated stratigraphy and astronomical tuning of the Loulja sections (Bou Regreg area, NW Morocco). Paleoceanography 21, PA3011. https://doi.org/10.1029/2005PA001193.

Vasiliev, I., Mezger, E.M., Lugli, S., Reichart, G.J., Manzi, V., Roveri, M., 2017. How dry was the Mediterranean during the Messinian salinity crisis? Palaeogeogr. Palaeoclimatol. Palaeoecol. 471, 120–133. https://doi.org/10.1016/j.paleo.2017.01.032.

Warren, J.K., 2016. Evaporites: A Geological Compendium. Springer.

Further reading

Garcia-Castellanos, D., Villaseñor, A., 2011. Messinian salinity crisis regulated by competing tectonics and erosion at the Gibraltar arc. Nature 480, 359–363. https://doi.org/10.1038/nature10651.

Mancini, A.M., Gennari, R., Natalicchio, M., Pierre, F.D., Carnevale, G., Pastero, L., Pellegrino, L., Pilade, F., Lozar, F., 2022. Taphonomic bias on calcareous micro and nannofossils and paleoenvironmental evolution across the Messinian Salinity Crisis onset: insights from the Sorbas Basin (SE Spain). Palaeogeogr. Palaeoclimatol. Palaeoecol. 111056. https://doi.org/10.1016/j.palaeo.2022.111056.